

ABSTRACT

Title of Thesis: EFFECTS OF DRIVE SPEED MODULATION
 ON DYNAMICS OF SLENDER
 ROTATING STRUCTURES

Abdullah Al-Zibdeh, 2016

Thesis directed by: Professor Balakumar Balachandran
 Department of Mechanical Engineering

Slender rotating structures are used in many mechanical systems. These structures can suffer from undesired vibrations that can affect the components and safety of a system. Furthermore, since some these structures can operate in a harsh environment, installation and operation of sensors that are needed for closed-loop and collocated control schemes may not be feasible. Hence, the need for an open-loop non-collocated scheme for control of the dynamics of these structures. In this work, the effects of drive speed modulation on the dynamics of slender rotating structures are studied.

Slender rotating structures are a type of mechanical rotating structures, whose length to diameter ratio is large. For these structures, the torsion mode natural frequencies can be low. In particular, for isotropic structures, the first few torsion mode frequencies can be of the same order as the first few bending mode frequencies. These situations can be conducive for energy transfer amongst bending and torsion modes. Scenarios with torsional vibrations experienced by rotating structures with

continuous rotor-stator contact occur in many rotating mechanical systems. Drill strings used in the oil and gas industry are an example of rotating structures whose torsional vibrations can be deleterious to the components of the drilling system. As a novel approach to mitigate undesired vibrations, the effects of adding a sinusoidal excitation to the rotation speed of a drill string are studied. A portion of the drill string located within a borewell is considered and this rotating structure has been modeled as an extended Jeffcott rotor and a sinusoidal excitation has been added to the drive speed of the rotor. After constructing a three-degree-of-freedom model to capture lateral and torsional motions, the equations of motions are reduced to a single differential equation governing torsional vibrations during continuous stator contact. An approximate solution has been obtained by making use of the Method of Direct Partition of Motions with the governing torsional equation of motion. The results showed that for a rotor undergoing forward or backward whirling, the addition of sinusoidal excitation to the drive speed can cause an increase in the equivalent torsional stiffness, smooth the discontinuous friction force at contact, and reduce the regions of negative slope in the friction coefficient variation with respect to speed. Experiments with a scaled drill string apparatus have also been conducted and the experimental results show good agreement with the numerical results obtained from the developed models. These findings suggest that the extended Jeffcott rotordynamics model can be useful for studies of rotor dynamics in situations with continuous rotor-stator contact. Furthermore, the results obtained suggest that the drive speed modulation scheme can have value for attenuating drill-string vibrations.

EFFECTS OF DRIVE SPEED MODULATION ON DYNAMICS
OF SLENDER ROTATING STRUCTURES

by

Abdullah Al-Zibdeh

Thesis submitted to the Faculty of the Graduate School of the
University of Maryland, College Park in partial fulfillment
of the requirements for the degree of
Master of Science
2016

Advisory Committee:

Professor Balakumar Balachandran, Chair and Advisor, Department of Mechanical
Engineering

Professor Amr Baz, Department of Mechanical Engineering

Assistant Professor Jin-Oh Hahn, Department of Mechanical Engineering

© Copyright by
Abdullah Al-Zibdeh
2016

Acknowledgments

I would like to thank Professor Balachandran, my advisor and committee chair, for his support and guidance during my graduate studies. I would also like to thank my committee members, Professor Baz and Professor Hahn, for their assistance in completing this thesis.

I want to thank all of my other colleagues in the Dynamics and Vibrations Group for their support and help. Finally, I would like to thank my family and friends for their support and love.

I also would like to gratefully acknowledge the support received from the Qatar National Research Fund for NPRP Project 7-083-2-041, to pursue this collaborative work between the University of Maryland, College Park, MD, USA and Qatar University, Doha, Qatar.

Table of Contents

List of Figures	v
List of Abbreviations	viii
1 Introduction and Background	1
1.1 Drill-String Vibrations	2
1.2 Whirling Motions of Drill Strings	3
1.3 Drill-String Modeling	4
1.4 Drill-String Experimental Studies	6
1.5 Control of Drill-String Vibrations	8
1.6 High Frequency Excitation	9
1.7 Contributions	10
1.8 Organization of Thesis	11
2 Modeling, Analytical, and Numerical Studies	12
2.1 Jeffcott Rotor Model and Governing Equations	13
2.2 Continuous Rotor-Stator Contact and Reduction of Order	17
2.3 Non-Dimensionalization	19
2.4 High Frequency Excitation	21
2.5 Forward Whirling	22
2.5.1 Approximate Solution	23
2.6 Backward Whirling	31
2.6.1 Approximate Solution	34
2.6.1.1 Approximate Solution for Slow Whirl Speed	34
2.6.1.2 Approximate Solution for Fast Whirl Speeds	38
3 Experimental Studies	42
3.1 Experimental Setup	42
3.2 Forward Whirling	43
3.2.1 Torsion Vibrations	43
3.2.2 Lateral Vibrations	49
3.3 Backward Whirling	53

3.3.1	Torsion Vibrations	53
3.3.2	Hysteresis	57
3.3.3	Lateral Vibrations	61
4	Summary and Future Work	66
4.1	Summary and Conclusions	66
4.2	Recommendations For Future Work	68
A	MATLAB Codes	70
	Bibliography	78

List of Figures

1.1	Schematic of a drill rig [1].	2
1.2	Whirling of drill strings. (a) Definitions used in describing the response, (b) forward whirling without contact, (c) forward whirling with contact, and (d) backward whirling with contact. Adapted from [2].	4
2.1	Extended Jeffcott Rotor Model: (a) Static configuration and (b) Dynamic configuration (during continuous rotor-stator contact).	14
2.2	Modulated drive variation. Here, $\Omega = 60$ rpm, $A = 0.1\Omega = 6$ rpm, and $\alpha = 10\Omega = 10$ Hz.	22
2.3	Comparison between results from the full (top) and the reduced order (bottom) models during forward whirling without drive speed modulation and $\Omega = 0.9(2\pi)$ rad/s. (a) Time histories and (b) Frequency spectra.	25
2.4	Comparison between results from the full (top) and the reduced order (bottom) models during forward whirling with drive speed modulation $\Omega = 0.9(2\pi)$ rad/s, $\alpha = 7.2(2\pi)$ rad/s, and $A = 0.1\Omega$. (a) Time histories and (b) Frequency spectra.	26
2.5	Simulations of the reduced-order system (equation (2.22)) during forward whirling and the approximate solution (equation (2.34)) for $\tilde{\Omega} = 0.42$, $\tilde{\alpha} = 10\tilde{\Omega}$, and $\tilde{A} = 0.1\tilde{\Omega}$	29
2.6	Change in friction coefficient with high frequency excitation during forward whirling.	30
2.7	Comparison between results from the full (top) and the reduced order (bottom) models during backward whirling without drive speed modulation for $\Omega = 0.7(2\pi)$ rad/s, and $\gamma = 3.1(2\pi)$ rad/s. (a) Time histories and (b) Frequency spectra.	32
2.8	Comparison between results from the full (top) and the reduced order (bottom) models during backward whirling with drive speed modulation for $\Omega = 0.7(2\pi)$ rad/s, $\gamma = 3.1(2\pi)$ rad/s, and $\alpha = 8\gamma = 25.2(2\pi)$ rad/s. (a) Time histories and (b) Frequency spectra.	33
2.9	Time histories of the approximate solution and the original equation result for $\tilde{\Omega} = 0.3$, $\tilde{\alpha} = 10\tilde{\gamma}$, and $\tilde{A} = 0.1\tilde{\Omega}$	37

2.10	Change in effective friction coefficient $\tilde{\mu}(\tilde{v}_{rel})$ with and without high frequency excitation during backward whirling and slow whirl speeds.	37
2.11	Time histories of the approximate solution and the original equation result for $\tilde{\Omega} = 0.87$, $\tilde{\gamma} = 3.3$, $\tilde{\alpha} = 10\tilde{\gamma}$, and $\tilde{A} = 0.1\tilde{\Omega}$	40
2.12	Change in effective friction coefficient $\tilde{\mu}(\tilde{v}_{rel})$ with and without high frequency excitation during backward whirling and fast whirl speeds.	41
3.1	Experimental arrangement, adapted from [3].	43
3.2	Comparison between time responses obtained from the simulations (top) and experiments (bottom) at a drive frequency of $\Omega = 0.9(2\pi)$ <i>rad/s</i> with $A = 0$ during forward whirling.	45
3.3	Comparison between Fast Fourier Transforms (FFTs) of the responses obtained from the simulations (top) and experiments (bottom) at a drive frequency of $\Omega = 0.9(2\pi)$ <i>rad/s</i> with $A = 0$ during forward whirling.	46
3.4	Comparison between time responses obtained from the simulations (top) and experiments (bottom) at a drive frequency of $\Omega = 0.9(2\pi)$ <i>rad/s</i> with $A = 0.1\Omega$ and $\alpha = 7.2(2\pi)$ <i>rad/s</i> during forward whirling.	46
3.5	Comparison between Fast Fourier Transforms (FFTs) of the responses obtained from the simulations (top) and experiments (bottom) at a drive frequency of $\Omega = 0.9(2\pi)$ <i>rad/s</i> with $A = 0.1\Omega$ and $\alpha = 7.2(2\pi)$ <i>rad/s</i> during forward whirling.	47
3.6	Normalized Fourier spectra of torsion displacement response during forward whirling. a) Simulations and b) Experiments.	48
3.7	Comparison of the rotor center x -deflection obtained from the simulations (top) and experiments (bottom) at a drive frequency of $\Omega = 0.9(2\pi)$ <i>rad/s</i> with $A = 0$ during forward whirling.	49
3.8	Comparison of Fast Fourier Transforms (FFTs) of the rotor center x -deflection obtained from the simulations (top) and experiments (bottom) at a drive frequency of $\Omega = 0.9(2\pi)$ <i>rad/s</i> with $A = 0$ during forward whirling.	50
3.9	Whirl orbit during forward whirling with $\Omega = 0.9(2\pi)$ <i>rad/s</i> . a) Simulations and b) Experiments.	50
3.10	Comparison of the rotor center x -deflection obtained from the simulations (top) and experiments (bottom) at a drive frequency of $\Omega = 0.9(2\pi)$ <i>rad/s</i> , $A = 0.1\Omega$, and $\alpha = 7.2(2\pi)$ <i>rad/s</i> during forward whirling.	51
3.11	Comparison of Fast Fourier Transforms (FFTs) of the rotor center x -deflection obtained from the simulations (top) and experiments (bottom) at a drive frequency of $\Omega = 0.9(2\pi)$ <i>rad/s</i> , $A = 0.1\Omega$, and $\alpha = 7.2(2\pi)$ <i>rad/s</i> during forward whirling.	52
3.12	Whirl orbit during forward whirling with $\Omega = 0.9(2\pi)$ <i>rad/s</i> , $A = 0.1\Omega$, and $\alpha = 7.2(2\pi)$ <i>rad/s</i> . a) Simulations and b) Experiments.	52

3.13	Comparison between time responses obtained from the simulations (top) and experiments (bottom) at a drive frequency of $\Omega = 0.6(2\pi)$ <i>rad/s</i> with $A = 0$ during backward whirling.	55
3.14	Comparison between Fast Fourier Transforms (FFTs) of the responses obtained from the simulations (top) and experiments (bottom) at a drive frequency of $\Omega = 0.6(2\pi)$ <i>rad/s</i> with $A = 0$ during backward whirling.	55
3.15	Comparison between time responses obtained from the simulations (top) and experiments (bottom) at a drive frequency of $\Omega = 0.6(2\pi)$ <i>rad/s</i> with $A = 0.1\Omega$ and $\alpha = 16.2(2\pi)$ <i>rad/s</i> during backward whirling.	56
3.16	Comparison between Fast Fourier Transforms (FFTs) of the responses obtained from the simulations (top) and experiments (bottom) at a drive frequency of $\Omega = 0.6(2\pi)$ <i>rad/s</i> with $A = 0.1\Omega$ and $\alpha = 16.2(2\pi)$ <i>rad/s</i> during backward whirling.	56
3.17	Normalized Fourier spectra of the torsion displacement response during backward whirling. a) Simulations and b) Experiments.	58
3.18	Change in the maximum amplitude of torsion displacement during a sweep-up, sweep-down test during backward whirling.	60
3.19	Frequency spectra of torsion displacement during a sweep-up, sweep-down test during backward whirling (bold lines correspond to the down-sweep).	60
3.20	Time history of torsion amplitude during a jump at a drive speed of 39 rpm.	61
3.21	Comparison of the rotor center x -deflection obtained from the simulations (top) and experiments (bottom) at a drive frequency of $\Omega = 0.67(2\pi)$ <i>rad/s</i> with $A = 0$ during backward whirling.	62
3.22	Comparison of Fast Fourier Transforms (FFTs) of the rotor center x -deflection obtained from the simulations (top) and experiments (bottom) at a drive frequency of $\Omega = 0.67(2\pi)$ <i>rad/s</i> with $A = 0$ during backward whirling.	62
3.23	Whirl orbit during backward whirling with $\Omega = 0.67(2\pi)$ <i>rad/s</i> . a) Simulations and b) Experiments.	63
3.24	Comparison of the rotor center x -deflection obtained from the simulations (top) and experiments (bottom) at a drive frequency of $\Omega = 0.67(2\pi)$ <i>rad/s</i> with $A = 0.1\Omega$, and $\alpha = 16.2(2\pi)$ <i>rad/s</i> during backward whirling.	64
3.25	Comparison of Fast Fourier Transforms (FFTs) of the rotor center x -deflection obtained from the simulations (top) and experiments (bottom) at a drive frequency of $\Omega = 0.67(2\pi)$ <i>rad/s</i> with $A = 0.1\Omega$, and $\alpha = 16.2(2\pi)$ <i>rad/s</i> during backward whirling.	64
3.26	Whirl orbit during backward whirling with $\Omega = 0.67(2\pi)$ <i>rad/s</i> , $A = 0.1\Omega$, and $\alpha = 16.2(2\pi)$ <i>rad/s</i> . a) Simulations and b) Experiments.	65

List of Abbreviations

x	Lateral x-direction deflection
y	Lateral y-direction deflection
θ	Torsional deflection
ω_{nt}	Torsional natural frequency
ω_{nb}	Bending natural frequency
M	Rotor mass
m	Mass imbalance
J	Rotor moment of inertia
e	Eccentricity of mass imbalance
δ	Rotor-stator clearance
k_b	Drill-string lateral stiffness
k_t	Drill-string torsion stiffness
k_s	Stator stiffness
c_b	Drill-string lateral damping
c_t	Drill-string torsion damping
ζ_b	Bending damping ratio
ζ_t	Torsion damping ratio
Ω	Motor drive speed
$\dot{G}(t)$	Drive speed modulation function
α	Drive speed modulation frequency
A	Drive speed modulation amplitude
μ	Coefficient of friction
v_{rel}	Relative speed at point of contact
Ω	Motor rotational frequency
$\omega_{fwd,bwd}$	Rotor whirl frequency
γ	Relative whirl frequency
a	Rotor radius to rotor-stator clearance ratio
MDPM	Method of Direct Partition of Motions
DOF	Degree of Freedom
HFE	High Frequency Excitation
FFT	Fast Fourier Transform

Chapter 1: Introduction and Background

Slender rotating structures, which are rotating structures that have a large length to diameter ratio, are used in many engineering applications. An example of such structures is drill strings that are used in the oil and gas industry. Drill strings are long sections that contain the drill pipe, bottom hole assembly, drilling tools, and the drill bit. Drill strings are used to transmit torque from the top drive to the drill bit, and to transmit drilling fluid that is used to prevent fluids from entering the well bore by providing hydrostatic pressure and to cool the drill bit. A schematic of a drilling rig is shown in Figure 1.1.

During normal drilling operations, drill strings can impact the borehole and under certain circumstances, they can remain in continuous contact with it. The nonlinear nature of drill string and borehole contact, and the generated forces from the drill bit can significantly affect and alter the dynamics of a drill string. Therefore, studying the dynamics of slender rotating structures during continuous rotor-stator contact is important to improve our understanding of drill-string dynamics.

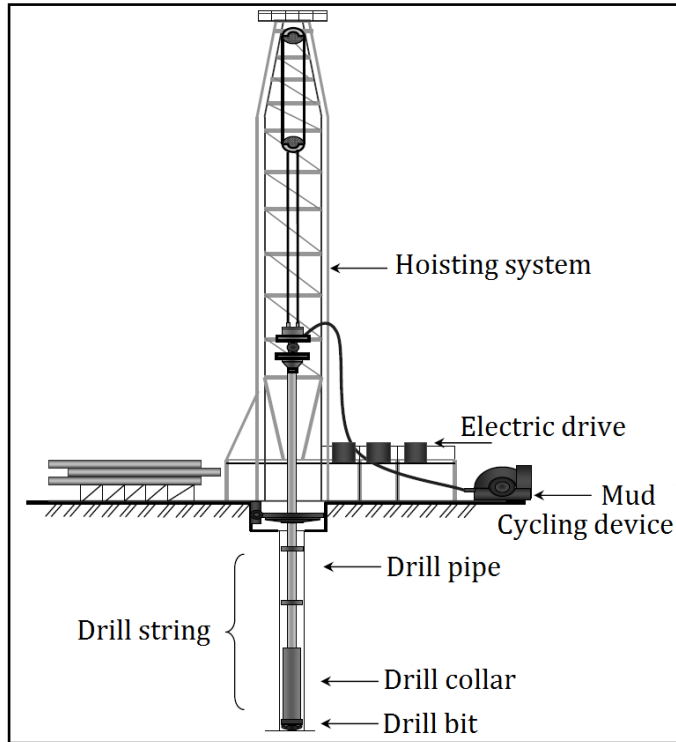


Figure 1.1: Schematic of a drill rig [1].

1.1 Drill-String Vibrations

Due to the large length to diameter ratio of drill strings, the first bending and torsional natural frequencies can be close to each other. With appropriate coupling, this frequency relationship can lead to energy transfer between the associated vibration modes. Additionally, drill strings exhibit many nonlinear phenomena due to the nonlinear nature of the interaction of the drill string with the surrounding environment. These interactions can cause the drill string to undergo impact motions with the borehole that can excite torsional, lateral, and axial modes and push the drill string into undesired and destructive types of motions.

Drill strings can impact the borehole and remain in contact with the borehole

while in rotation. These whirling motions are nonlinear due to friction and contact forces between the drill string and the borehole, and due to the fluid forces that arise from the presence of the high pressure drilling fluids. Additionally, drill strings can undergo stick-slip motions, which are a form of self-excited vibrations, that can cause a drill string to store and release torsional energy. These vibrations can excite oscillations close to the natural frequencies of the system and cause large torsional, lateral, and axial deformations, which can significantly damage the drill string and the drilling equipment.

1.2 Whirling Motions of Drill Strings

Under certain circumstances, drill strings can impact the borehole and remain in contact with it. This causes the drill string to undergo whirling motions. Two types of whirling motions exist for drill strings; namely, forward and backward whirling. Forward whirling is a state wherein the drill string rotates in the same direction as that of the rotation of the top drive, while backward whirling is a state in which the drill string rotates in the opposite direction to that of the top drive. During forward whirling and continuous contact between the drill string and borehole, a drill string continuously slips (rubs) against the borehole. However, during backward whirling, a drill string can rotate with or without slipping against the borehole. If the ratio of the drill string diameter to the clearance between the drill string and the borehole is small, a drill string may rotate much faster than the prescribed drive speed. This can be extremely dangerous and damaging to the

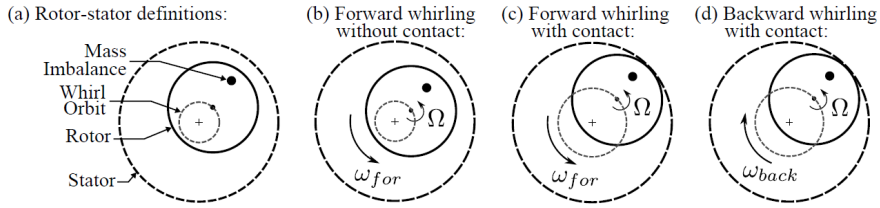


Figure 1.2: Whirling of drill strings. (a) Definitions used in describing the response, (b) forward whirling without contact, (c) forward whirling with contact, and (d) backward whirling with contact. Adapted from [2].

drilling equipment and is a major cause of failure of drill strings. An illustration of different types of motion is shown in Figure 1.2.

Both forward and backward whirling can cause large lateral deformations in the drill string. Torsional vibrations can be excited in both types of motion due to the coupling of lateral and torsional modes, friction forces, and nonlinear forces transmitted from the drill bit. Furthermore, backward whirling is considered to be much more dangerous than forward whirling due to the excessive speeds at which the drill string can whirl.

1.3 Drill-String Modeling

Modeling drill strings have been an active area of research for researchers and engineers. These modeling efforts have been further challenged by advancements in drilling technologies such as directional drilling and horizontal drilling. Drill-string models range from a simple one degree-of-freedom model to more complicated six degree-of-freedom, finite-element, and distributed-parameter models. Simple models

are easy to derive and study but due to many assumptions, these models cannot accurately predict the drill-string dynamics. Therefore, the level of details and complexity of a dynamic model depends on the purpose of the study and the tools available.

Multiple models have been developed to separately investigate torsional, lateral, or axial vibrations. For example, Jansen [4], proposed a lateral mass-spring rotor model to study lateral vibrations. Kreisly and Vance [5] developed a longitudinal vibrations model and studied the effect of shock on the longitudinal vibrations of a drill string. Jansen and Steen [6] studied self-excited torsion vibrations in drill strings with a torsion drill string model and applied an active vibration damping approach to damp self-excited torsion vibrations.

Since the three modes of vibrations in drill strings are coupled, models that account for coupling between two or more modes of vibrations are very important. For example, Sampaio, Piovan, and Lozano [7] presented a nonlinear model that accounts for the coupling of axial and torsional vibrations. Coupling between axial and lateral vibrations in drill strings were studied by Yigit and Christoforou [8]. Vlajic, Liao, Karki, and Balachandran [3] derived a coupled lateral-torsion reduced order model that exhibits stick-slip motions.

In addition to modeling the structure of drill strings, another important part is modeling the interaction between a drill string and borehole. Proper modeling of the contact forces is crucial because these forces cause drill strings to undergo whirling and stick-slip motions, which can affect the operation of the drilling equipment.

Friction forces and consequently the generated torque on the drill string are

known to depend on the relative velocity at the point of contact between the drill string and the borehole. Therefore, models that have a velocity dependent friction parameter have been widely used in the literature. Additionally, models that account for fluid forces also provide additional insights into the dynamics of drill strings under normal operating conditions. For example, Leine, Van Campen, and Keultjes [9] studied nonlinear dynamics and bifurcations of drill strings by using a piecewise angular velocity torque function and included fluid forces in the study. Kreuzer and Steidl [10] used a friction model with a velocity weakening effect to model the contact between the drill string and the borehole. Additionally, Vljajic, Liao, Karki, and Balachandran [3, 11] studied a similar system and used a friction model with velocity weakening and Stribeck effect.

1.4 Drill-String Experimental Studies

Full-scale test rigs such as the Catoosa Geophysical and Drilling Technology Testing and Evaluation Facility (CTF) are used in the drilling industry to study the dynamics of drill strings and drilling equipment, and to study the interactions between the drilling equipment and the borehole. In addition to full-scale test rigs, scaled experimental drilling apparatuses are also used widely to validate theoretical results and to test the applicability of different control schemes. The benefits of scaled drill string arrangements are derived from the means they provide in a relatively inexpensive and accessible way to investigate the dynamics of drill strings. A brief description of some experimental scaled drill string arrangements is provided

in this section.

Mihajlovic [12] studied torsional and lateral vibrations with a scaled drill string experiment. This setup consists of two vertical rotors connected by a drill string that is driven by a DC motor. Additionally, a brake at the bottom disk is used to add a torque input to the drill string and an oil-box is constructed in order to add oil to the brake. This lubrication aids the existence of torsional vibrations in the setup. Furthermore, lateral vibrations are excited by an unbalanced mass at the lower disk.

Researchers in the dynamics and vibrations group at the University of Maryland, College Park have built a 25:1 scaled down version of a vertical drill string system in terms of the string diameter [13]. The setup consists of two disks, one at the top and one at the bottom with encoders attached at both ends. A mass imbalance is attached to the bottom disk that is enclosed within a fixed steel stator. The stator is used to represent the borehole and to study the interactions between the drill string and the borehole.

A modified version of the scaled drill-string apparatus used by Liao, Vlajic, Karki, and Balachandran [13] was presented by Vlajic *et al.* [14]. The setup consists of an aluminum rod connected to a servomotor through a chuck at the top and to a rotor at the bottom that is enclosed by a steel stator to account for the drill string and borehole interactions. Additionally, by connecting the drill string to a horizontal shaker, Vlajic, Fitzgerald, Nguyen, and Balachandran [15] studied the dynamics of drill strings in configurations that are not vertical.

More recently, Westermann, Gorelik, Rudat, Moritz, Neubauer, Wallaschek,

and Hohn [16] presented a new scaled rig for analyzing drill-string vibrations. This setup consists of a horizontal rotating shaft supported by fixed and floating bearings. The authors showed that this setup can be used to study stick-slip vibrations, forward and backward whirling, and snaking motions of drill strings.

1.5 Control of Drill-String Vibrations

A large number of research publications have focused on controlling torsional vibrations and stick-slip motions. Jensen and Van den Steen [6] used feedback control at the rotary table to actively damp self-excited torsional vibrations. Karkoub, Zribi, Elchaar, and Lamont [17] developed a controller using robust μ synthesis. Serrarens, Vande Molengraft, Kok, and Van den Steen [18] developed an H_∞ controller. Christoforu and Yigit [19] studied state feedback control with a drill-string model that allowed for coupling amongst axial, torsion, and lateral motions. Hidabbi, Samanta, and Seibi [20] studied a non-linear controller for minimizing torsional and lateral vibrations of a drill string. A more recent approach to control the torsional vibrations of drill strings has been proposed by Kreuzer and Steidl [21] based on decomposition of traveling waves through sensor measurements close to the top drive. Finally, Meyer [22] numerically and experimentally investigated the effects of sinusoidal drive speed modulation on slender rotating structures without contact forces and showed that drive speed modulation can alter the dynamic response of the rotating structure.

1.6 High Frequency Excitation

High frequency excitations (HFEs) can have many effects on nonlinear mechanical systems. For example, a vertical pendulum can be stabilized in the upside down position by vertically exciting the support with a high frequency input [23]. Dry friction can be smoothed, and consequently, the resulting dissipation behavior can be similar to that obtained with viscous damping that has many engineering applications, for example, in transportation of mass (e.g., granular material) [24]. Furthermore, a high frequency excitation can change the equivalent stiffness of a mechanical system.

Many other studies have considered the effects of high frequency excitation on mechanical systems. Blekhman [24] discussed many applications and nontrivial effects of HFE, and a useful mathematical apparatus for HFE (the Method of Direct Partition of Motions). Thomsen [25] studied a mass on a moving belt that can undergo self-excited vibrations and showed that a high frequency excitation can effectively cancel the negative friction slope, and consequently help quench self-excited oscillations. Thomsen [26], provided some examples of the effects of high frequency excitation on the slow dynamics of mechanical systems such as stiffening, biasing, and smoothening.

The effects of high frequency excitation on many mechanical systems suggest that applying the concept to rotating drill strings might have a beneficial effect and could possibly quench stick-slip oscillations that can be harmful to drill strings.

1.7 Contributions

A main purpose of this thesis study has been to explore the effects of modulating the motor drive speed on the dynamics of a slender rotating structure during continuous rotor-stator contact with applications to drill strings. In this study, a novel approach has been proposed to mitigate stick-slip vibrations in rotating structures during continuous rotor-stator contact. The proposed method differs from previous control efforts in that the control is open loop and does not depend on any measurements along the drill string or rotary table; thus, helping avoid installation costs and sensors durability and reliability problems.

The proposed method relies on the idea that a high frequency excitation can be used to quench self-excited vibrations in mechanical systems. Therefore, in this thesis, first, modulation of the drive speed is applied to an extended Jeffcott rotor model and a reduced order equation governing torsion motions during continuous rotor-stator contact is derived. Then an approximate solution has been obtained to study the effects of high frequency excitation on the torsion dynamics and the contact characteristics for both forward and backward whirling during continuous rotor-stator contact.

Additionally, experimental work has been carried out and the results are used to study the effects of drive speed modulation on a slender rotating structure experiencing continuous rotor-stator contact. Results obtained from the experiments are then used to study the validity of the extended Jeffcott rotor model used in this thesis and in the work of Vlajic, Liu, Karki, and Balachandran [11].

This thesis builds upon the work conducted by previous students in the same research group at the University of Maryland, College Park, namely, the studies of Liao [13] , Vljic [2], and Meyer [22].

1.8 Organization of Thesis

The organization of this thesis is as follows. In Chapter 2, a model is derived for a slender rotating structure during continuous rotor-stator contact and drive speed modulation; then, a reduced order equation governing torsional vibrations is obtained. The effects of high frequency excitation are then investigated by deriving approximate solutions for both forward and backward whirling cases. Experimental studies obtained with a scaled drill-string experiment are presented in Chapter 3. Results obtained for continuous rotor-stator contact and drive speed modulation are compared to the numerical results obtained in Chapter 2. Summary and future work are provided in Chapter 4 along with concluding remarks. Finally, the codes used in this work are presented in the appendix.

Chapter 2: Modeling, Analytical, and Numerical Studies

In this chapter, the drill string has been modeled as an extended Jeffcott rotor with three degrees of freedom, and a sinusoidal modulation is added to the drive speed. Proceeding along the lines of the group's prior work [11], it is assumed that the rotor is in continuous contact with the stator. The three degree-of-freedom (DOF) system is reduced to a single second-order nonlinear differential equation governing the torsional motion during forward whirling in the first section, and backward whirling in the second section. To further analyze the response during continuous rotor-stator contact, the reduced order model is non-dimensionalized and an approximate solution has been obtained by using the Method of Direct Partition of Motions. This method allows the separation of slow scale motions from fast scale motions. The resultant semi-analytic solution is compared with the solution of the original full system and it is seen that the Method of Direct Partition of Motions is able to provide an approximate solution that compares well with the numerical results obtained through direct integration of the original equations. Finally, the effects of high frequency excitation on the torsional dynamics are discussed.

2.1 Jeffcott Rotor Model and Governing Equations

The Jeffcott rotor model (named after Jeffcott 1919) is widely used in studying rotating systems. This simplified rotor system accounts for lateral deformation and has two degrees of freedom, namely, the x -displacement and y -displacement of the center of the rotor. For the current study, the drill string is modeled as an extended Jeffcott rotor to account for the torsional vibrations; an illustrative system representation is shown in Figure 2.1(a). The rotor has a radius R , mass M , and an unbalanced mass m with eccentricity e . The rotary inertia of the rotor and the mass imbalance about the center of the rotor is $J = J_o + me^2$ where J_o is the inertia of the rotor without the unbalanced mass. The center of the rotor coincides with the center of the stator, and the clearance between the rotor and stator is δ . The rotor is assumed to be symmetric so that the equivalent lateral stiffness is $k_x = k_y = k_b$ and the torsion stiffness is k_t . Similarly, the lateral damping is assumed to be symmetric $c_x = c_y = c_b$, and the torsion damping is c_t . Additionally, the stator has a stiffness of k_s . A schematic of the rotor at an instant of time t and the coordinate axes are shown in Figure 2.1(b). The torsional displacement of the rotor is θ , and the angular displacement is given by $\beta = \theta(t) + \Omega t + G(t)$, where Ω is the motor base drive speed, and the time derivative of $G(t)$ is the drive speed modulation function. For the case of sinusoidal drive speed modulation $\dot{G}(t) = A \sin(\alpha t)$, where this sinusoidal excitation has an amplitude of A [rad/s] and frequency of α [rad/s]. The rotor is assumed to be planar and does not experience gyroscopic effects, and that gravity is acting normal to the $x - y$ plane. Lagrange's equations are used to

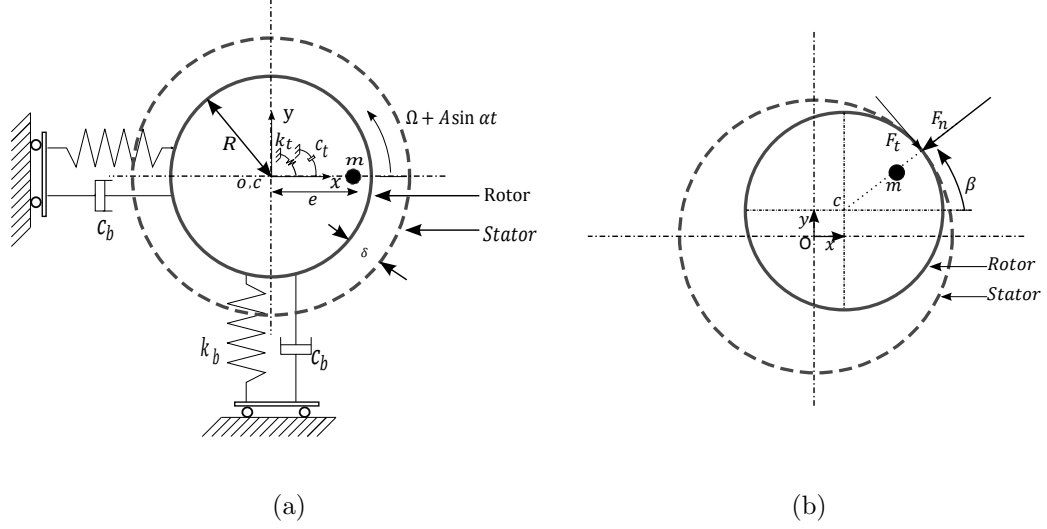


Figure 2.1: Extended Jeffcott Rotor Model: (a) Static configuration and (b) Dynamic configuration (during continuous rotor-stator contact).

determine the equations of motion of the system, and the kinetic energy of the rotor is given by

$$KE = \frac{1}{2}M(\dot{x}^2 + \dot{y}^2) + \frac{(J_o\dot{\beta}^2)}{2} + \frac{m}{2}[(\dot{x} - e\dot{\beta} \sin \beta)^2 + (\dot{y} + e\dot{\beta} \cos \beta)^2] \quad (2.1)$$

Here, the overdots represent derivatives with respect to time. The potential energy is given by

$$PE = \frac{1}{2}[k_b x^2 + k_b y^2 + k_t \theta^2] \quad (2.2)$$

The Rayleigh dissipation function is expressed as

$$D = \frac{1}{2}[c_b \dot{x}^2 + c_b \dot{y}^2 + c_t \dot{\theta}^2] \quad (2.3)$$

Then, by using Lagrange's equation, the equations of motion are obtained as

$$(M + m)\ddot{x} + c_b\dot{x} + k_b x = me[\ddot{\beta} \sin(\beta) + \dot{\beta}^2 \cos(\beta)] + F_x \quad (2.4)$$

$$(M + m)\ddot{y} + c_b\dot{y} + k_b y = me[-\ddot{\beta} \cos(\beta) + \dot{\beta}^2 \sin(\beta)] + F_y \quad (2.5)$$

$$J\ddot{\theta} + c_t\dot{\theta} + k_t\theta = me[\ddot{x} \sin(\beta) - \ddot{y} \cos(\beta)] - J\ddot{G}(t) + M_t \quad (2.6)$$

Following the contact model and forces presented in Vlajic *et al.* [11], during motion, the contact forces will be zero until the amplitude of rotation $\Gamma = \sqrt{x^2 + y^2}$, becomes equal to the clearance δ . Then, the normal force acting on the rotor at the point of contact is

$$F_n = \begin{cases} 0 & \text{for } \Gamma \leq \delta \\ k_s(\Gamma - \delta) & \text{for } \Gamma > \delta \end{cases} \quad (2.7)$$

and the friction force is

$$F_t = -\mu F_n \quad (2.8)$$

The moment is

$$M_t = F_t R \quad (2.9)$$

Decomposing the normal and tangential components along the x - and y -directions, the forces, and moment acting on the rotor are given by

$$F_x = \frac{F_t y - F_n x}{\Gamma}, \quad F_y = \frac{F_t x - F_n y}{\Gamma}, \quad M_t = -F_t R \quad (2.10)$$

To capture the stick-slip phenomenon, a friction model with the Stribeck effect and discontinuity at zero relative velocity is adapted from Leine *et al.* [27], Thomsen [23], and Vlajic *et al.* [11]. This model is given by

$$\begin{aligned}
\mu(v_{rel}) &= \mu_s \operatorname{sgn}(v_{rel}) - \frac{3}{2} \left(\frac{\mu_s - \mu_m}{v_m} \right) v_{rel} + \frac{1}{2} \left(\frac{\mu_s - \mu_m}{v_m^3} \right) v_{rel}^3 \\
&= \mu_s \operatorname{sgn}(v_{rel}) - \mu_1 v_{rel} + \mu_3 v_{rel}^3
\end{aligned} \tag{2.11}$$

Here, μ_s is the static friction coefficient, and μ_m is the minimum friction coefficient at $v_{rel} = v_m$.

The friction model used in equation (2.11) causes the system to become stiff about the point $v_{rel} = 0$, and consequently poses difficulties when numerically integrating the system. Therefore, as in Vlajic *et al* [11], during numerical integration, equation (2.11) is replaced with:

$$\mu(v_{rel}) = \mu_s \frac{2}{\pi} \arctan(\delta_f v_{rel}) - \mu_1 v_{rel} + \mu_3 v_{rel}^3 \tag{2.12}$$

where for large $\delta_f \gg 1$, equation (2.12) closely resembles the friction model of equation (2.11).

The relative speed between the rotor and stator at the point of contact is given by

$$v_{rel} = \left(\Omega + \dot{\theta} + \dot{G}(t) \right) R - \frac{\dot{x}y}{\Gamma} + \frac{\dot{y}x}{\Gamma} \tag{2.13}$$

Additionally, Vlajic *et al.* [3] determined numerically and experimentally that the following whirl frequency relations hold for a range of drive speeds:

$$\omega = a\Omega, \quad \omega_{fwd} \approx \Omega, \quad \omega_{back} \approx -\Omega \frac{R}{\delta} \tag{2.14}$$

Note that for the rest of this thesis, $a = 1$ will be used for the forward whirling case, and $a = -\frac{R}{\delta}$ will be used for the backward whirling case.

In equation (2.14), ω_{fwd} is the forward whirling frequency and ω_{back} is the backward whirling frequency. The negative sign in the backward whirling frequency is due to the rotation being in the opposite direction of the drive rotation. Additionally, for systems with $R > \delta$, the backward whirling frequency ω_{back} will be larger than the prescribed drive frequency Ω in magnitude.

2.2 Continuous Rotor-Stator Contact and Reduction of Order

Studies of torsional vibrations during continuous rotor-stator contact are important. Therefore, to further analyze the torsional motion, the full order extended Jeffcott rotor model given in equations (2.4)-(2.6) will be reduced to a single degree-of-freedom differential equation governing torsional motion.

During continuous rotor-stator contact, the forces acting on the rotor are found by performing a force balance on the rotor leading to

$$F_n = [M\delta + m(\delta + e \cos \phi_{ubm})] a^2 \left(\Omega + \dot{G}(t) \right)^2 - k_b \delta \quad (2.15)$$

This was found previously in Vljajic *et al.* [11] without the drive speed modulation term. ϕ_{ubm} is the angle between the unbalanced mass and the line of action of the normal force. If the eccentricity is much smaller than the clearance and the unbalanced mass is much smaller than the rotor mass, which is usually the case in most rotor systems, equation (2.15) can be approximated as

$$F_n = (M + m)\delta a^2 \left(\Omega + \dot{G}(t) \right)^2 - k_b \delta \quad (2.16)$$

When the rotor maintains contact with the stator, the x - and y -displacements can be reduced to

$$x = \delta \cos(a(\Omega t + G(t))) \quad (2.17)$$

$$y = \delta \sin(a(\Omega t + G(t))) \quad (2.18)$$

During continuous contact, the amplitude of torsional vibrations is small; therefore, $\sin \theta$ and $\cos \theta$ can be approximated by the first term of their respective Taylor series expansion. This assumption holds for most rotor systems, if the amplitude of torsional vibrations is small. Therefore, $\sin \beta$ and $\cos \beta$ can be simplified to:

$$\sin \beta = \sin(\theta + \Omega t + G(t)) \approx \theta \cos(\Omega t + G(t)) + \sin(\Omega t + G(t)) \quad (2.19)$$

$$\cos \beta = \cos(\theta + \Omega t + G(t)) \approx \cos(\Omega t + G(t)) - \theta \sin(\Omega t + G(t)) \quad (2.20)$$

After substituting back equations (2.16)-(2.20) into equations (2.4)-(2.6), the equation governing torsional vibration during continuous rotor-stator contact becomes

$$\begin{aligned}
& J\ddot{\theta} + c_t\dot{\theta} + \left\{ k_t - me \left[\ddot{G}(t)\delta a \sin((a-1)(\Omega t + G(t))) \right. \right. \\
& \left. \left. - \delta a^2(\Omega + \dot{G}(t))^2 \cos((a-1)(\Omega t + G(t))) \right] \right\} \theta \\
& = me \left[\delta a^2(\Omega + \dot{G}(t))^2 \sin((a-1)(\Omega t + G(t))) \right. \\
& \left. - \delta a \ddot{G}(t) \cos((a-1)(\Omega t + G(t))) \right] - \ddot{G}(t)J + M_t
\end{aligned} \tag{2.21}$$

During forward whirling, the whirl frequency is approximately equal to the drive frequency $a = 1$, and during backward whirling, $a = -\frac{R}{\delta}$.

2.3 Non-Dimensionalization

To further study the torsional response during forward and backward whirling with sinusoidal drive speed modulation, \dot{G} is replaced by $A \sin \alpha t$ and equation (2.21) is rewritten in a non-dimensional form as

$$\begin{aligned}
& \ddot{\theta} + 2\zeta\dot{\theta} + \theta \left[1 + \tilde{m} \left(a(\tilde{\Omega} + \tilde{A} \sin \tilde{\alpha} \tilde{t})^2 \cos((a-1)(\tilde{\Omega} \tilde{t} - \frac{\tilde{A}}{\tilde{\alpha}} \cos \tilde{\alpha} \tilde{t})) \right. \right. \\
& \left. \left. - \tilde{A} \tilde{\alpha} \cos(\tilde{\alpha} \tilde{t}) \sin((a-1)(\tilde{\Omega} \tilde{t} - \frac{\tilde{A}}{\tilde{\alpha}} \cos \tilde{\alpha} \tilde{t})) \right) \right] \\
& = \tilde{m} \left[a(\tilde{\Omega} + \tilde{A} \sin \tilde{\alpha} \tilde{t})^2 \sin((a-1)(\tilde{\Omega} \tilde{t} - \frac{\tilde{A}}{\tilde{\alpha}} \cos \tilde{\alpha} \tilde{t})) \right. \\
& \left. - \tilde{A} \tilde{\alpha} \cos(\tilde{\alpha} \tilde{t}) \cos((a-1)(\tilde{\Omega} \tilde{t} - \frac{\tilde{A}}{\tilde{\alpha}} \cos \tilde{\alpha} \tilde{t})) \right] - \tilde{A} \tilde{\alpha} \cos \tilde{\alpha} \tilde{t} + \frac{M_t}{J\omega_n^2}
\end{aligned} \tag{2.22}$$

Here, the non-dimensional parameters in equation (2.22) are given by

$$\begin{aligned}
\tilde{m} &= \frac{\delta mea}{J}, & \tilde{\Omega} &= \frac{\Omega}{\omega_{nt}}, & \tilde{\alpha} &= \frac{\alpha}{\omega_{nt}} & \tilde{\gamma} &= (a-1)\tilde{\Omega} \\
\tilde{A} &= \frac{A}{\omega_{nt}}, & \tilde{t} &= \omega_{nt}t, & \omega_{nt} &= \sqrt{\frac{k_t}{J}} & 2\zeta &= \frac{c}{\omega_{nt}J} \\
\tilde{n}_1 &= \frac{m+M}{J}\delta R, & \tilde{n}_2 &= \frac{k_b\delta R}{J\omega_n^2}
\end{aligned}$$

The relative speed has different values depending on whether it is forward or backward whirling. During forward whirling and continuous rotor-stator contact, the rotor continuously rubs against the stator surface and the relative speed becomes

$$v_{rel} = (\delta + R)(\Omega + A \sin \alpha t) + \dot{\theta}R \quad (2.23)$$

The relative speed between the rotor and stator during forward whirling can be non-dimensionalized by dividing throughout by $\omega_{nt}R$, leading to

$$\tilde{v}_{rel} = \dot{\theta} + \left(\tilde{\Omega} + \tilde{A} \sin \tilde{\alpha} \tilde{t} \right) \tilde{c}, \quad \tilde{c} = \frac{R + \delta}{R} \quad (2.24)$$

During backward whirling and continuous rotor-stator contact, under the assumption of no-slip conditions, which means that the relative velocity between the rotor and the stator is zero in the absence of torsional vibrations, the non-dimensional relative speed becomes

$$\tilde{v}_{rel} = \dot{\theta} \quad (2.25)$$

For a high frequency addition, $\tilde{\alpha} \gg \tilde{\Omega}$ and $\tilde{A} < \tilde{\Omega}$; therefore, the $(\tilde{\Omega}\tilde{t} - \frac{\tilde{A}}{\tilde{\alpha}} \cos \tilde{\alpha}\tilde{t})$ term can be approximated by $(\tilde{\Omega}\tilde{t})$, which will be used from this point forward. Additionally, the radius to clearance ratio a is set according to the whirling motion;

that is, $a = 1$ for forward whirling and $a = -\frac{R}{\delta}$ for backward whirling.

Furthermore, the non-dimensional moment can be written in terms of the abovementioned non-dimensional parameters as

$$\tilde{M}_t = -(\tilde{n}_1 a^2 (\tilde{\Omega} + \tilde{A} \sin \tilde{\alpha} \tilde{t})^2 - \tilde{n}_2) \quad (2.26)$$

2.4 High Frequency Excitation

As discussed in the introductory chapter, high frequency excitations can have many interesting effects on nonlinear mechanical systems. Drill-string motions are influenced by discontinuous friction forces, and these rotating structures can suffer from self-excited (stick-slip) vibrations. Therefore, because high frequency excitation can smooth the friction coefficient variation with relative speed at the point of contact, the inclusion of a high frequency excitation in the drive input might provide a way to mitigate the unwanted stick-slip vibrations. For that reason, the effects of high frequency excitation on the torsion dynamics of the rotor system during continuous rotor-stator contact are studied next.

In the present case, a high frequency excitation is added to the current system by having the modulation frequency be much larger than the first torsion natural frequency of the system; that is, $\alpha \gg \omega_{nt}$. For this modulation to be realistically applicable, the modulation amplitude is set to be reasonably lower than the drive speed; that is, $A < \Omega$. An example of a modulated drive speed input is shown in Figure 2.2.

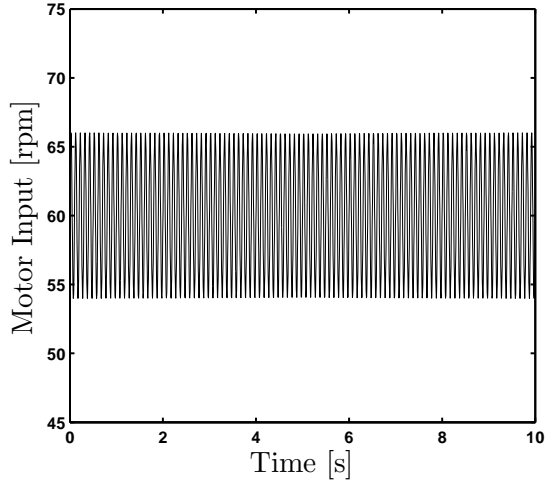


Figure 2.2: Modulated drive variation. Here, $\Omega = 60$ rpm, $A = 0.1\Omega = 6$ rpm, and $\alpha = 10\Omega = 10$ Hz.

2.5 Forward Whirling

During forward whirling, the rotor whirls in the same direction as the drive rotation, and during continuous contact and drive speed modulation, the torsional equation of motion becomes

$$J\ddot{\theta} + c_t\dot{\theta} + \theta[m\epsilon\delta(\Omega + A\sin\alpha t)^2] = -(m\epsilon\delta + J)A\alpha\cos\alpha t + M_t \quad (2.27)$$

A comparison between the responses obtained from the full system (equations (2.4) - (2.6)) with rotor-stator contact and the reduced order model (equation (2.27)), with and without high frequency excitation is shown in Figures 2.3 and 2.4. The time histories and Fast Fourier Transforms were used to compare results obtained from both models, and a circular whirl orbit confirms that the rotor is in continuous contact with the stator in the full system. The parameters used in

the simulations have been chosen according to the corresponding parameters of the experimental setup and these parameters are given in Table 2.1. Additionally, the equivalent torsion stiffness and lateral stiffness have been obtained from the natural frequencies of the corresponding vibration modes according to $k_b = \omega_{nb}^2(M + m)$ and $k_t = \omega_{nt}^2 J$.

The stable solution of equation (2.27) can suffer a loss of stability through a Hopf bifurcation for small damping and slow drive speed Ω . A more detailed study of this case has been discussed in the work of Vlajic *et al.* [11].

2.5.1 Approximate Solution

To gain more insights into the effects of high frequency excitation on the slow dynamics of the rotor system and on the friction variation with relative speed, an approximate solution of equation (2.22) during continuous rotor-stator contact will be constructed using the Method of Direct Partition of Motions (MDPM) [23, 24]. This method is suitable for systems with excitation frequencies away from the main system resonances and for components that are undergoing rapid oscillations. When this method is applied, the differential equation is separated into two subsets: one describing slow components and one describing fast components.

To apply the Method of Direct Partition of Motions, fast excitations through the drive input are considered; that is, $\tilde{\alpha} \gg \tilde{\Omega}$ and $\tilde{\alpha} \gg 1$. Then the non-dimensional

Table 2.1: Parameter values used in simulations and experiments

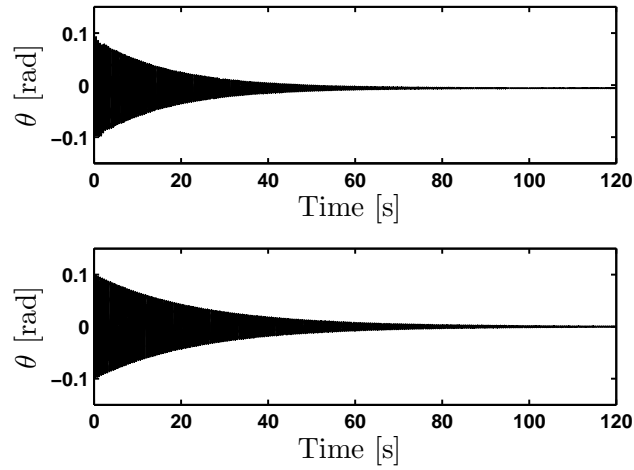
Parameter	Value	Units
ζ_b	0.01	-
ζ	0.0032	-
e	0.0635	m
M	0.625	kg
m	0.08	kg
ω_{nb}	$0.51(2\pi)$	rad/s
ω_{nt}	$2.1(2\pi)$	rad/s
k_s	$1e^5$	N/m
R	0.088	m
v_m	0.6	m/s
δ	0.023	m
δ_f	$1e^6$	-
μ_s	$1.3 \mu_m$	-
μ_m	0.005	-
Ω	$(0.6 - 1.2)(2\pi)$	rad/s
A	$(0 - 0.3)\Omega$	rad/s

torsional motion $\theta(\tilde{t})$ is separated into slow and fast components as

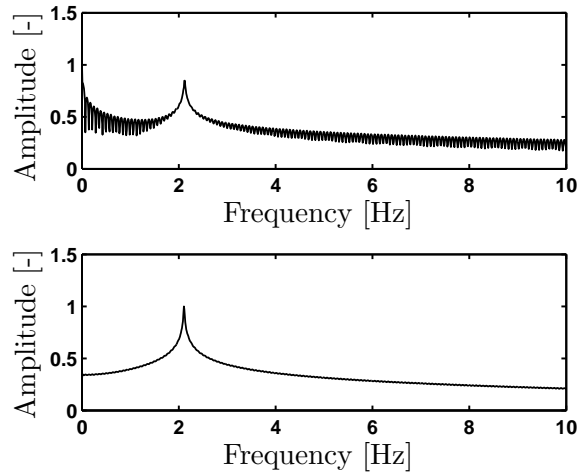
$$\theta(\tilde{t}, \tau) = z(\tilde{t}) + \tilde{\alpha}^{-1}\varphi(\tilde{t}, \tau) \quad (2.28)$$

Here, $z(\tilde{t})$ represents the slow components and $\varphi(\tilde{t}, \tau)$ represents the fast components. Here \tilde{t} represents the slow time scale while $\tau = \tilde{\alpha}\tilde{t}$ represents the fast time scale.

Due to the addition of an extra scale, for the transformation to be unique, one needs to impose the constraint that the fast-time average of the fast motion $\varphi(\tilde{t}, \tau)$



(a)

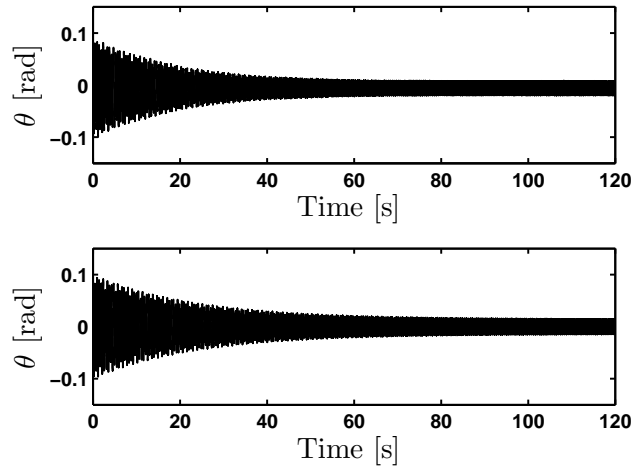


(b)

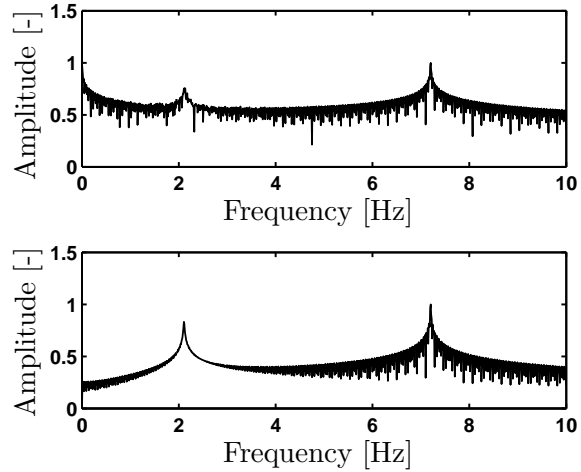
Figure 2.3: Comparison between results from the full (top) and the reduced order (bottom) models during forward whirling without drive speed modulation and $\Omega = 0.9(2\pi)$ *rad/s*. (a) Time histories and (b) Frequency spectra.

is zero; that is,

$$\langle \varphi(\tilde{t}, \tau) \rangle = \frac{1}{2\pi} \int_0^{2\pi} \varphi(\tilde{t}, \tau) d\tau = 0 \quad (2.29)$$



(a)



(b)

Figure 2.4: Comparison between results from the full (top) and the reduced order (bottom) models during forward whirling with drive speed modulation $\Omega = 0.9(2\pi)$ rad/s , $\alpha = 7.2(2\pi)$ rad/s , and $A = 0.1\Omega$. (a) Time histories and (b) Frequency spectra.

The first and second derivatives of θ with respect to the slow time scale \tilde{t} are

given by

$$\dot{\theta} = \dot{z} + \tilde{\alpha}^{-1}\dot{\varphi} + \varphi' \quad (2.30)$$

$$\ddot{\theta} = \tilde{\alpha}\varphi'' + \ddot{z} + 2\dot{\varphi}' + \tilde{\alpha}^{-1}\ddot{\varphi} \quad (2.31)$$

Here, the overdot represents the derivative with respect to the slow time scale \tilde{t} and the prime represents the derivative with respect to the fast time scale τ .

On substituting back into equation (2.27) and rearranging the terms in powers of α , the result is

$$\begin{aligned} \varphi'' = & -(\tilde{m} + 1)\tilde{A} \cos \tau - \tilde{\alpha}^{-1} \left[\ddot{z} + 2\dot{\varphi}' + 2\zeta\dot{z} + 2\zeta\dot{\varphi}' + z[1 + (\tilde{m} + 1)(\tilde{\omega} + \tilde{A} \sin \tau)^2] \right. \\ & \left. + (\tilde{n}_1(\tilde{\omega} + \tilde{A} \sin \tau)^2 - \tilde{n}_2)\tilde{\mu}(\tilde{v}_{rel}) \right] - \tilde{\alpha}^{-2} \left[\ddot{\varphi} + 2\zeta\dot{\varphi} + [1 + (\tilde{m} + 1)(\tilde{\omega} + \tilde{A} \sin \tau)^2]\varphi \right] \end{aligned} \quad (2.32)$$

Integrating the dominant terms twice with respect to τ gives the fast motion term; one obtains

$$\varphi = (\tilde{m} + 1)\tilde{A} \cos \tau \quad (2.33)$$

which satisfies the constraint $\langle \varphi(\tilde{t}, \tau) \rangle = 0$.

The equation of motion governing slow motion is obtained by averaging the $\mathcal{O}(\alpha^{-1})$ terms in equation (2.32) over one period of fast motion. Note that the slow displacement z and slow time \tilde{t} are considered stationary relative to the fast time scale; therefore, they are considered constants in the integration. Consequently, the averaged equation governing slow motion becomes

$$\begin{aligned}
\ddot{z} + 2\zeta\dot{z} + z + \frac{1}{2}(\tilde{m} + 1) (\tilde{A}^2 + 2\tilde{\Omega}) z &= \tilde{n}_2 \left[\tilde{f} - \tilde{\mu}_1 \tilde{B} + \frac{1}{2} \tilde{\mu}_3 \tilde{B} (3\tilde{H}^2 \tilde{A}^2 + 2\tilde{B}^2) \right] \\
- \frac{\tilde{n}_1 \tilde{\mu}_1}{2} \left[2\tilde{\Omega}^2 \tilde{B} + \tilde{A}^2 (\dot{z} + 3\tilde{c}\tilde{\Omega} - 4(\tilde{m} + 1)\tilde{\Omega}) \right] \\
- \frac{\tilde{n}_1 \tilde{\mu}_3}{8} \left[8\tilde{\Omega}^2 \tilde{B}^3 + 3\tilde{A}^4 \tilde{H}^2 (3\dot{z} + 5\tilde{c}\tilde{\Omega} - 4(\tilde{m} + 1)\tilde{\Omega}) \right] \\
- 4\tilde{A}^2 (\dot{z} + \tilde{c}\tilde{\Omega}) \left[\dot{z} + 4(2\tilde{c} - 3(\tilde{m} + 1)) \dot{z}\tilde{\Omega} + 2(5\tilde{c}^2 - 12\tilde{c}\tilde{m} + 6(\tilde{m} + 1)^2) \tilde{\Omega}^2 \right] - \tilde{n}_1 \tilde{g}
\end{aligned} \tag{2.34}$$

Here

$$\tilde{B} = \dot{z} + \tilde{c}\tilde{\Omega} \quad \tilde{H} = \tilde{c} - 2(\tilde{m} + 1) \quad \tilde{P} = \sqrt{\frac{\tilde{H}^2 \tilde{A}^2 - \tilde{B}^2}{\tilde{H}^2 \tilde{A}^2}}$$

and

$$\tilde{f} = \begin{cases} \mu_s \operatorname{sgn}(\tilde{B}) & \text{for } \tilde{B} \geq \tilde{H}\tilde{A} \\ \mu_s \left[-\frac{2}{\pi} \arcsin\left(\frac{\tilde{B}}{-\tilde{H}\tilde{A}}\right) \right] & \text{for } \tilde{B} < \tilde{H}\tilde{A} \end{cases}$$

$$\tilde{g} = \begin{cases} \mu_s \operatorname{sgn}(\tilde{B}) \left[\frac{\tilde{A}^2}{2} + \tilde{\Omega}^2 \right] & \text{for } \tilde{B} \geq \tilde{H}\tilde{A} \\ \frac{\mu_s}{4\tilde{H}\pi^2} \left[\tilde{A} \left(4\tilde{H}\tilde{\Omega} - \tilde{P}(\dot{z} - 3\tilde{c}\tilde{\Omega} + 8(\tilde{m} + 1)\tilde{\Omega}) \right) + \tilde{H}(\tilde{A}^2 + 2\tilde{\Omega}^2) \arcsin\left(\frac{\tilde{B}}{\tilde{H}\tilde{A}}\right) \right] & \text{for } \tilde{B} < \tilde{H}\tilde{A} \end{cases}$$

The total torsion response during forward whirling and high frequency excitation is then obtained by substituting the solution of equation (2.34) and the fast motion from equation (2.33) back into equation (2.28).

A comparison between the response obtained from the main torsion equation (equation 2.21), the approximate response obtained from applying the Method of Direct Partition of Motions, and the effect of ignoring the fast term $\tilde{\alpha}^{-1}\varphi(\tilde{t}, \tau)$ in

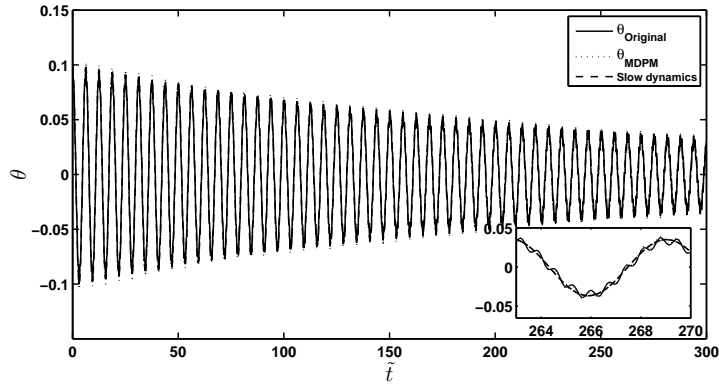


Figure 2.5: Simulations of the reduced-order system (equation (2.22)) during forward whirling and the approximate solution (equation (2.34)) for $\tilde{\Omega} = 0.42$, $\tilde{\alpha} = 10\tilde{\Omega}$, and $\tilde{A} = 0.1\tilde{\Omega}$.

the response are shown in Figure 2.5. As can be seen from Figure 2.5, the approximate solution is close to the response obtained from the original equation; also, the fast term $\tilde{\alpha}^{-1}\varphi(\tilde{t}, \tau)$ in equation (2.34) can be neglected without compromising the validity of the solution.

In equation (2.34), the modulation of the drive speed caused the effective torsion stiffness on the slow scale to increase from $k_{eff} = 1$ to $k_{eff} = 1 + \frac{\tilde{m}}{2}(2\tilde{\Omega}^2 + \tilde{A}^2)$ during forward whirling. The stiffening effect is due to two parts, the first part, $\tilde{m}\tilde{\Omega}^2$ is due to the drive speed that is known to exist for many rotor systems and the second stiffening term, $\frac{\tilde{m}\tilde{A}^2}{2}$ that is due to the high frequency excitation.

The average friction coefficient can be found by substituting the non-dimensional relative velocity given by equation (2.24) into the friction model given in equation (2.11) and integrating the friction coefficient over one period of the fast time scale τ . The averaged friction coefficient is of the form

$$\langle \tilde{\mu}(v_{rel}) \rangle = \tilde{f} - \tilde{\mu}_1 \tilde{B} + \frac{1}{2} \tilde{\mu}_3 \tilde{B} \left(3\tilde{A}^2 \tilde{H}^2 + 2\tilde{B}^2 \right) \quad (2.35)$$

Here, \tilde{f} , \tilde{B} , and \tilde{H} are the same as in (2.34). It is apparent from the *arcsin* function in equations (2.35) and (2.34) that the high frequency excitation causes the slope of the friction coefficient about the discontinuity to be smoothed and reduces the regions of negative friction slope, which can cause instabilities and self-excited vibrations. A comparison of the friction model with and without high frequency excitation for forward whirling is shown in Figure 2.6. Additionally, the discontinuity position shifts to the left with increasing drive speed $\tilde{\Omega}$. This shift can be related to the dependence of the relative velocity on the drive speed as well as on the high frequency excitation.

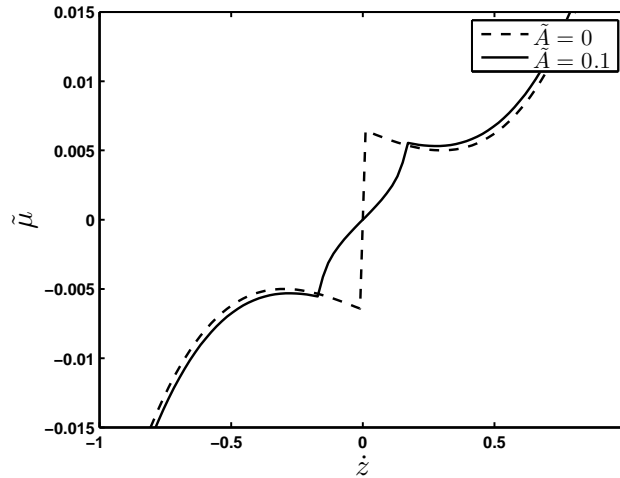


Figure 2.6: Change in friction coefficient with high frequency excitation during forward whirling.

2.6 Backward Whirling

During continuous rotor-stator contact and backward whirling, the whirling frequency with drive speed modulation is (assuming no-slip condition)

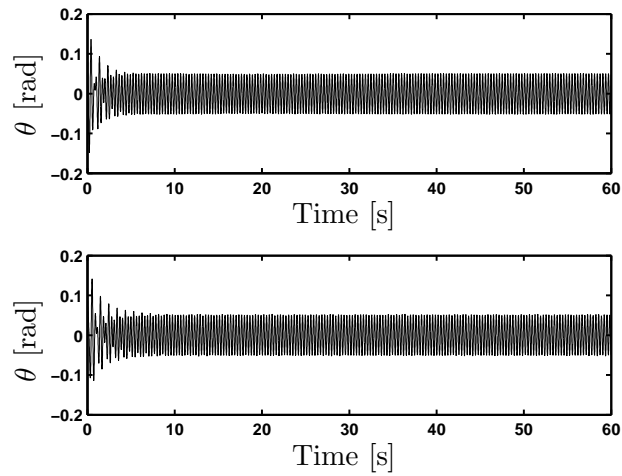
$$\omega_{back} = -\frac{R}{\delta} (\Omega + A \sin \alpha t) = a (\Omega + A \sin \alpha t) \quad (2.36)$$

From equation (2.21) with $a = -\frac{\delta}{R}$ and $\dot{G} = A \sin(\alpha t)$, one obtains the following second-order nonlinear differential equation governing torsional motion during backward whirling with continuous rotor-stator contact:

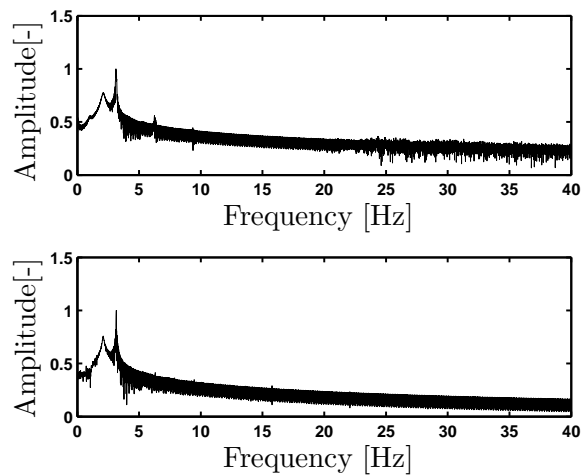
$$\begin{aligned} & J\ddot{\theta} + c_t\dot{\theta} + \theta \left\{ k_t + me \left[\delta a^2 (\Omega + A \sin \alpha t)^2 \cos \left((a-1) \left(\Omega t - \frac{A}{\alpha} \cos \alpha t \right) \right) \right. \right. \\ & \left. \left. - A\alpha\delta a \cos \alpha t \sin \left((a-1) \left(\Omega t - \frac{A}{\alpha} \cos \alpha t \right) \right) \right] \right\} \\ & = me \left[\delta a^2 (\Omega + A \sin \alpha t)^2 \sin \left((a-1) \left(\Omega t - \frac{A}{\alpha} \cos \alpha t \right) \right) \right. \\ & \left. - A\alpha\delta a \cos \alpha t \cos \left((a-1) \left(\Omega t - \frac{A}{\alpha} \cos \alpha t \right) \right) \right] - JA\alpha \cos \alpha t + M_t \end{aligned} \quad (2.37)$$

A comparison between the responses obtained from the full model (equations (2.4-2.6)) during backward whirling with continuous rotor-stator contact and the reduced order equation for backward whirling, with and without high frequency excitation is shown in Figures 2.7 and 2.8. Time histories and Fast Fourier Transforms are used to compare the results obtained from both models. The figures show that the full and reduced order models have the same dominant frequencies at $|\gamma| = |a-1|\Omega$, where γ is the relative whirl speed, and another peak at the excitation frequency α . However, the reduced order model results contain two frequency

components at $\alpha \pm |\gamma|$, which were not present in the full model results.

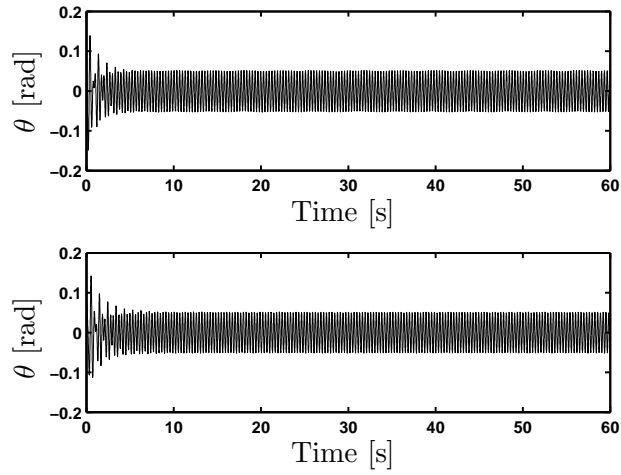


(a)

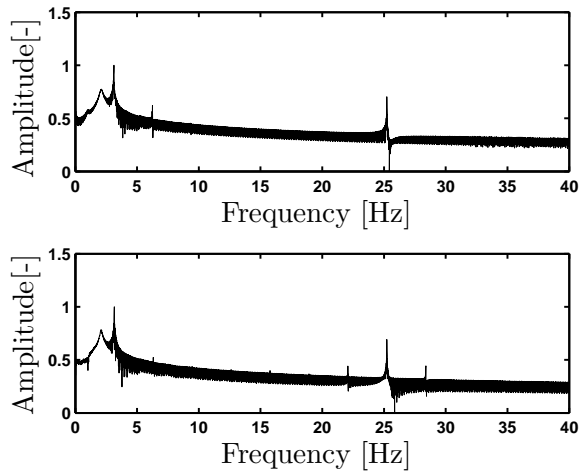


(b)

Figure 2.7: Comparison between results from the full (top) and the reduced order (bottom) models during backward whirling without drive speed modulation for $\Omega = 0.7(2\pi)$ *rad/s*, and $\gamma = 3.1(2\pi)$ *rad/s*. (a) Time histories and (b) Frequency spectra.



(a)



(b)

Figure 2.8: Comparison between results from the full (top) and the reduced order (bottom) models during backward whirling with drive speed modulation for $\Omega = 0.7(2\pi) \text{ rad/s}$, $\gamma = 3.1(2\pi) \text{ rad/s}$, and $\alpha = 8\gamma = 25.2(2\pi) \text{ rad/s}$. (a) Time histories and (b) Frequency spectra.

2.6.1 Approximate Solution

Similar to the case of forward whirling, an approximate semi-analytic solution for equation (2.22) during backward whirling has been constructed by using the Method of Direct Partition of Motions. As in the case of forward whirling, this method is suitable for the analysis of systems modulated with a high frequency excitation (HFE). For the case of backward whirling, two cases are considered. The first case is low speed backward whirling with HFE. The whirl speed is considered to be of the same order as the first torsion natural frequency and the drive speed is modulated by a frequency that is much higher than the first torsion natural frequency. The second case is high speed backward whirling. The whirl speed as well as the excitation frequency are higher than the first torsion natural frequency.

2.6.1.1 Approximate Solution for Slow Whirl Speed

After introducing the fast time scale $\tau = \tilde{\alpha}\tilde{t}$, approximating the $(\tilde{\Omega}\tilde{t} - \frac{\tilde{A}}{\tilde{\alpha}} \cos \tilde{\alpha}\tilde{t})$ term by $(\tilde{\Omega}\tilde{t})$, and letting $\tilde{\gamma} = (a-1)\tilde{\Omega}$ be the non-dimensional relative whirl speed, then the non-dimensional torsional equation, Eq. (2.22) during backward whirling becomes

$$\begin{aligned}
& \ddot{\theta} + 2\zeta\dot{\theta} + \theta \left[1 + \tilde{m} \left(a(\tilde{\Omega} + \tilde{A} \sin \tau)^2 \cos(\tilde{\gamma}\tilde{t}) - \tilde{A}\tilde{\alpha} \cos \tau \sin(\tilde{\gamma}\tilde{t}) \right) \right] \\
& = \tilde{m} \left[a(\tilde{\Omega} + \tilde{A} \sin \tau)^2 - \tilde{A}\tilde{\alpha} \cos \tau \cos(\tilde{\gamma}\tilde{t}) \right] - \tilde{A}\tilde{\alpha} \cos \tau \\
& - \left(\tilde{n}_1 a^2 \left[\tilde{\Omega} + \tilde{A} \sin \tilde{\alpha}\tilde{t} \right]^2 - \tilde{n}_2 \right) \tilde{\mu} (\tilde{v}_{rel})
\end{aligned} \tag{2.38}$$

Applying the Method of Direct Partition of Motions, as in the case of forward whirling, the torsion displacement is separated into slow and fast components as follows:

$$\theta(\tilde{t}, \tau) = z(\tilde{t}) + \tilde{\alpha}^{-1}\varphi(\tilde{t}, \tau) \quad (2.39)$$

After substituting back into equation (2.38), and collecting the terms of the same powers of $\tilde{\alpha}$, one obtains

$$\begin{aligned} \varphi'' = & -[\tilde{A} \cos T + \tilde{A}\tilde{m} \cos \tilde{\gamma}\tilde{t} - \tilde{A}\tilde{m}z \cos \tau \sin \tilde{\gamma}\tilde{t}] - \tilde{\alpha}^{-1} \left[\ddot{z} + 2\zeta\dot{z} + 2\zeta\varphi' + 2\dot{\varphi}' \right. \\ & - \tilde{A}\tilde{m}\varphi \cos \tau \sin \tilde{\gamma}\tilde{t} + a\tilde{m}z \cos \tilde{\gamma}\tilde{t}(\tilde{\Omega} + \tilde{A} \sin \tau)^2 - a\tilde{m} \sin \tilde{\gamma}\tilde{t}(\tilde{\Omega} + \tilde{A} \sin \tau)^2 \\ & \left. + \left(\tilde{n}_1 [\tilde{\Omega} + \tilde{A} \sin \tau]^2 - \tilde{n}_2 \right) \tilde{\mu}(\tilde{v}_{rel}) \right] + O(\tilde{\alpha}^{-2}) \end{aligned} \quad (2.40)$$

Integrating the dominant term twice with respect to τ , the result is

$$\varphi = \tilde{A} \cos \tau [1 + \tilde{m} \cos \tilde{\gamma}\tilde{t} - \tilde{m}z \sin \tilde{\gamma}\tilde{t}] \quad (2.41)$$

Averaging the $\mathcal{O}(\tilde{\alpha}^{-1})$ terms in equation (2.40), one gets the differential equation governing slow torsional motion:

$$\begin{aligned} \ddot{z} + 2\zeta\dot{z} + z \left[1 + \frac{1}{2}a\tilde{m}(\tilde{A}^2 + 2\tilde{\Omega}^2) \cos \tilde{\gamma}\tilde{t} \right] = & \frac{1}{2} [\tilde{A}^2\tilde{m} + a\tilde{m}(\tilde{A}^2 + 2\tilde{\Omega}^2)] \sin \tilde{\gamma}\tilde{t} \\ & - \left\langle \left(\tilde{n}_1 [\tilde{\Omega} + \tilde{A} \sin \tau]^2 - \tilde{n}_2 \right) \tilde{\mu}(\tilde{v}_{rel}) \right\rangle \end{aligned} \quad (2.42)$$

To average the last term on the right hand side of equation (2.42), the discontinuous friction coefficient term is first expanded as a two-term Fourier series

expansion. Then, at low whirl speeds, the torsion variation magnitude is small. Therefore, it is possible to approximate the terms by their Taylor expansions around $\dot{z} = 0$. Then averaging the resulting terms, the equation governing slow motion for slow whirl speeds with high frequency modulation becomes

$$\begin{aligned}
\ddot{z} + 2\zeta\dot{z} + z\left[1 + \frac{1}{2}a\tilde{m}(\tilde{A}^2 + 2\tilde{\Omega}^2)\cos\tilde{\gamma}\tilde{t}\right] &= \frac{1}{2}\left[\tilde{A}^2\tilde{m} + a\tilde{m}(\tilde{A}^2 + 2\tilde{\Omega}^2)\right]\sin\tilde{\gamma}\tilde{t} \\
+ \frac{1}{2\pi}\dot{z}\left[\tilde{n}_2(16 - 2\pi\mu_1 + 3\tilde{A}^2\pi\mu_3) + a^2\tilde{n}_1(2(-8 + \pi\mu_1)\tilde{\Omega}^2 + \right. & \\
\tilde{A}^2(-8 + \pi\mu_1 - 3\pi\mu_3\tilde{\Omega}^2)) + 6\tilde{n}_1\tilde{n}_2\mu_3\tilde{A}^2\tilde{m}\pi(a^2\tilde{\Omega}^2)\cos\tilde{\gamma}\tilde{t}\left. \right] & \\
- \frac{1}{\pi}\tilde{n}_1a^2\tilde{A}^2\tilde{\Omega}(-8 + \pi\mu_1)(1 + \tilde{m}\cos\tilde{\gamma}\tilde{t} - z\tilde{m}\sin\tilde{\gamma}\tilde{t}) &
\end{aligned} \tag{2.43}$$

In equation (2.43), the whirl speed appears in both parametric and external excitation terms. An approximate solution can be determined by using perturbation analysis, and for the case of commensurate frequencies, the solution is expected to be periodic and Floquet analysis can be used to study the stability of the solution (e.g., see Nayfeh and Mook [28] and Nayfeh and Balachandran [29]).

A comparison between the solution obtained through the numerical simulations of equation (2.39) and equation (2.22) during backward whirling and a slow whirl speed is shown in Figure 2.9. As shown in the figures, there is a good correlation between the solutions obtained from both equations for a slow whirl speed.

The change in the friction coefficient for $\tilde{\Omega} = 0.3$ is shown in Figure 2.10. Similar to the case of forward whirling, the discontinuity at $\dot{z} = 0$ is smoothed and the regions where the friction coefficient has a negative slope have been reduced.

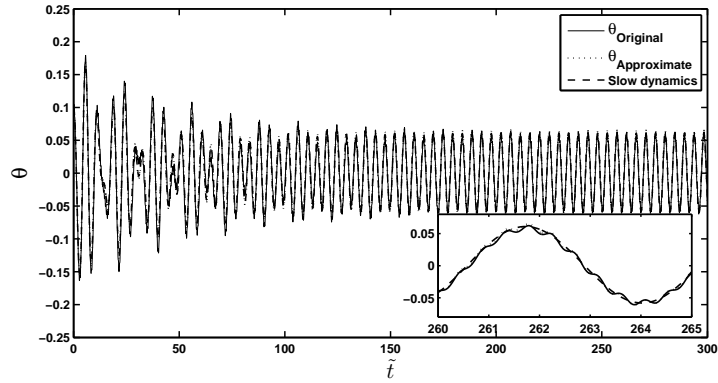


Figure 2.9: Time histories of the approximate solution and the original equation result for $\tilde{\Omega} = 0.3$, $\tilde{\alpha} = 10\tilde{\gamma}$, and $\tilde{A} = 0.1\tilde{\Omega}$.

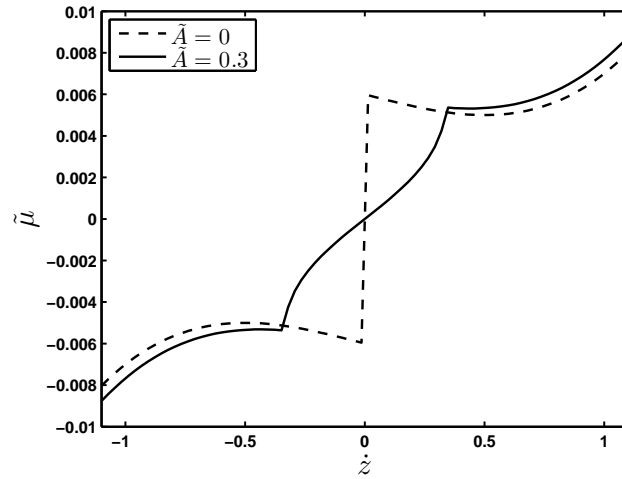


Figure 2.10: Change in effective friction coefficient $\tilde{\mu}(\tilde{v}_{rel})$ with and without high frequency excitation during backward whirling and slow whirl speeds.

2.6.1.2 Approximate Solution for Fast Whirl Speeds

A high frequency excitation during fast whirl speeds corresponds to the condition $\tilde{\gamma} = (a - 1)\tilde{\Omega} \gg 1$ and $\tilde{\alpha} \gg \tilde{\gamma}$. Due to the addition of the high frequency excitation, the differential equation governing slow motion will be sought in terms of two fast motions (or two fast time scales), $T = \tilde{\gamma}\tilde{t}$ for the fast whirl speed, and $\tau = \tilde{\alpha}\tilde{t}$ for the high frequency excitation. Then, the torsional displacement can be separated as follows:

$$\theta(\tilde{t}, T, \tau) = z(\tilde{t}, T) + \tilde{\alpha}^{-1}\varphi(\tilde{t}, T, \tau) \quad (2.44)$$

Additionally, for fast whirl speeds, one has

$$z(\tilde{t}, T) = s(\tilde{t}) + \tilde{\gamma}^{-1}\psi(\tilde{t}, T) \quad (2.45)$$

Here, $s(\tilde{t})$ represents the slow motion, and $\psi(\tilde{t}, T)$ represents the fast motion. Therefore, the torsion displacement can be expanded into two terms:

$$\theta(\tilde{t}, \tau, T) = s(\tilde{t}) + \tilde{\gamma}^{-1}\psi(\tilde{t}, T) + \tilde{\alpha}^{-1}\varphi(\tilde{t}, T, \tau) \quad (2.46)$$

In order for the expansion to be valid, two constraints should be satisfied:

$$\frac{1}{2\pi} \int_0^{2\pi} \psi(\tilde{t}, T) dT = 0, \quad \frac{1}{2\pi} \int_0^{2\pi} \varphi(\tilde{t}, T, \tau) d\tau = 0 \quad (2.47)$$

Starting from equation (2.38) and balancing the $\mathcal{O}(\tilde{\alpha}^n)$ terms, one gets the same formula for $\varphi(\tilde{t}, T)$ as in equation (2.41), after balancing the dominant $\mathcal{O}(\tilde{\gamma}^n)$ terms, one obtains the following equation for $\psi(\tilde{t}, T)$

$$\psi(\tilde{t}, T) = \frac{a\tilde{m}\tilde{\Omega}^2}{\tilde{\gamma}}(s \cos T - \sin T) \quad (2.48)$$

Integrating the $\mathcal{O}(\tilde{\alpha}^{-1})$ terms with respect to τ and then integrating the $\mathcal{O}(\tilde{\gamma}^{-1})$ terms of the resulting equation with respect to T , the result is the following equation governing torsional motion during fast whirl speeds and a high frequency excitation:

$$\begin{aligned} \ddot{s} + 2\zeta\dot{s} + s \left[1 + \frac{1}{4}\tilde{A}^2\tilde{m}^2 + \frac{1}{2}\frac{a^2\tilde{m}^2\tilde{\Omega}^4}{\tilde{\gamma}^2} \right] \\ = \left(\frac{1}{2\pi} \right)^2 \int_0^{2\pi} \int_0^{2\pi} (\tilde{n}_1 a^2 (\tilde{\Omega} + \tilde{A} \sin \tau)^2 - \tilde{n}_2) \tilde{\mu}(\tilde{v}_{rel}) d\tau dT \end{aligned} \quad (2.49)$$

here the friction function $\tilde{\mu}(\tilde{v}_{rel})$ is given by equation (2.11) and the non-dimensional relative velocity \tilde{v}_{rel} is of the form

$$\tilde{v}_{rel} = \frac{\partial s}{\partial \tilde{t}} + \frac{\partial \psi}{\partial T} + \frac{\partial \varphi}{\partial \tau} + \tilde{\gamma}^{-1} \frac{\partial \psi}{\partial \tilde{t}} + \tilde{\alpha}^{-1} \frac{\partial \varphi}{\partial \tilde{t}} \approx \frac{\partial s}{\partial \tilde{t}} + \frac{\partial \psi}{\partial T} + \frac{\partial \varphi}{\partial \tau} \quad (2.50)$$

The integral in equation (2.49) does not have a closed form solution; therefore, numerical integration of the integral will be used instead. During fast whirl speeds and a high frequency excitation, the effective stiffness of the torsion mode on the slow scale changed from $k_{eff} = 1$ to $k_{eff} = 1 + \frac{1}{4}\tilde{A}^2\tilde{m}^2 + \frac{1}{2}\frac{a^2\tilde{m}^2\tilde{\Omega}^4}{\tilde{\gamma}^2}$, which results from the high frequency excitation and the fast whirl speed. Vljajic *et al.* [11] obtained the same last term for the fast whirl speeds without a high frequency excitation.

A comparison between the solutions obtained through the numerical simulations of equation (2.45) and equation (2.22) during backward whirling and fast

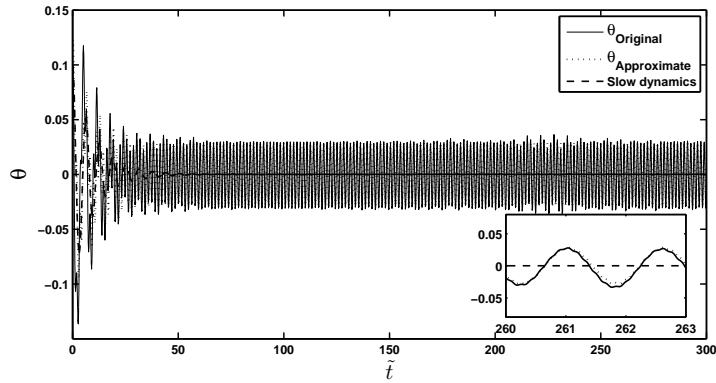


Figure 2.11: Time histories of the approximate solution and the original equation result for $\tilde{\Omega} = 0.87$, $\tilde{\gamma} = 3.3$, $\tilde{\alpha} = 10\tilde{\gamma}$, and $\tilde{A} = 0.1\tilde{\Omega}$

whirl speeds is shown in Figure 2.11. As can be seen in the figure, the approximate solution shows close resemblance to the solution obtained from the original torsional differential equation during backward whirling and fast whirl speeds and the presence of a high frequency excitation.

Vlajic *et al.* [11] showed that for fast whirl speeds the effective friction coefficient is smoothed about the discontinuity. The addition of a high frequency excitation showed that this smoothing effect can be enhanced and depends on both the whirl speed and the high frequency excitation amplitude. The change in the effective friction coefficient with and without high frequency excitation is shown in Figure 2.12.

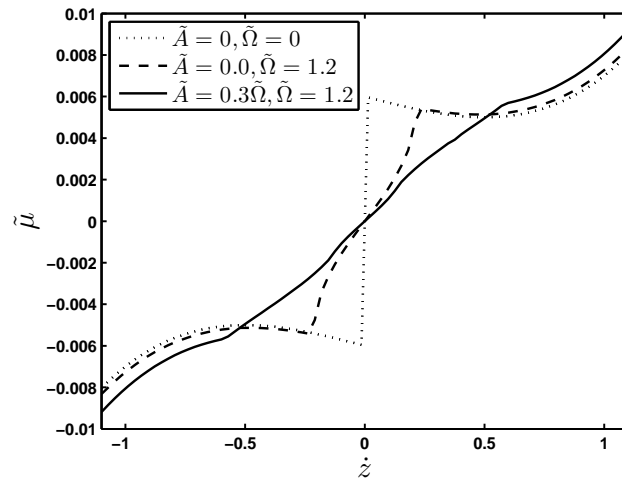


Figure 2.12: Change in effective friction coefficient $\tilde{\mu}(\tilde{v}_{rel})$ with and without high frequency excitation during backward whirling and fast whirl speeds.

Chapter 3: Experimental Studies

3.1 Experimental Setup

The experimental arrangement is shown in Figure 3.1. A servo motor is used to drive a shaft which represents the drill string, a rotor is attached to the other end of the shaft and is enclosed by a circular stator. The rotor represents the bottom hole assembly while the stator represents the borehole. A slip ring at the top of the shaft is used to connect the sensors with the data acquisition devices. Strain gages connected at the bottom of the shaft are used to get measure of torsion vibrations and a camera is used to track a white dot on the center of the rotor to get a measure of lateral vibrations of the bottom assembly. The measured data is fed through data acquisition modules to LabVIEW and then analyzed by using MATLAB software. Additionally, LabVIEW is used to modulate and control the drive speed of the servo motor.

When defining the parameters used in the simulations, the masses and dimensions of the corresponding experimental parts were measured and used in the numerical simulations. Additionally, because of difficulties in determining experimentally the values of the parameters used in the friction coefficient, multiple sets of torsion displacement data were generated during continuous rotor-stator contact

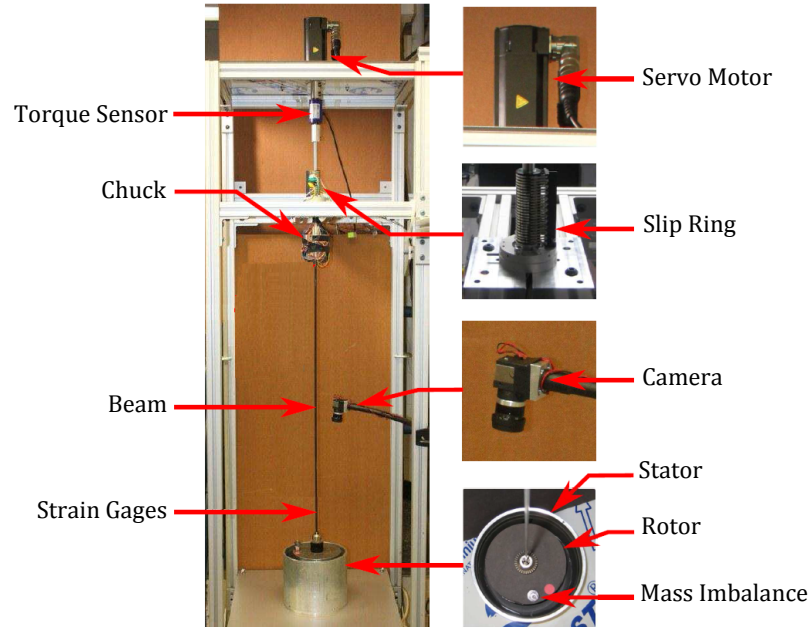


Figure 3.1: Experimental arrangement, adapted from [3].

and these time histories were compared to those of the simulations. The parameters of the friction coefficient in the numerical simulations were tweaked until very similar time histories were obtained.

3.2 Forward Whirling

3.2.1 Torsion Vibrations

The system was first studied at a constant drive speed to compare with as well as validate the predictions from the model given by equations (2.4)-(2.6) and the predictions from the reduced order model (equation (2.21)). Then the drive speed was modulated by adding a sinusoidal excitation similar to that used in the previous analytical study, and the results were compared to the previous findings. Multiple

tests were conducted for various secondary frequencies at speeds above 36 rpm due to the loss of contact between the rotor and stator at lower speeds. Additionally, at high rotation speeds, the rotor and stator sometimes disengage.

The motor drive frequency was first incrementally increased to $\Omega = 0.9(2\pi)$ *rad/s* which is a speed at which the rotor undergoes forward whirling with contact; then, a secondary excitation with a frequency of $\alpha = 7.2(2\pi)$ *rad/s* and amplitude of $A = 0.1\Omega$ was added to the motor drive speed. To compare the results obtained from the mathematical model (equation (2.21)) and the experiments, time histories and Fast Fourier Transforms (FFTs) were used. The Fast Fourier Transforms were obtained as ensemble averages of Fourier spectra obtained by using at least 30 data segments of 40 seconds each after steady state was reached. As seen in Figures 3.2 and 3.3, in the case of forward whirling without drive speed modulation, the simulations and experiments showed the same dominant peak at w_{nt} . However, the experimental results reveal multiple harmonics of the drive frequency ($\Omega = 0.9(2\pi)$ *rad/s*), mainly at 3.6 Hz, 5.4 Hz, 7.2 Hz, and 10.8 Hz, which were not present in the simulations.

A comparison between the results obtained from the experiments and the Jeffcott rotor model during forward whirling with drive speed modulation are shown in Figures 3.4 and 3.5. The results obtained from both simulations and experiments contained major peaks at $\omega_{nt} \approx 2.1(2\pi)$ *rad/s* and at $\alpha = 7.2(2\pi)$ *rad/s*. Similar to the case without drive speed modulation, the experiments contained significant peaks in the frequency spectrum at several harmonics of the drive speed.

Due to the the nature of contact in the experiment, motor noise, nonlinearities

and discontinuities in the friction between the rotor and the stator, motions at the bending natural frequency $\omega_{nb} \approx 0.51(2\pi) \text{ rad/s}$ and other frequency components were excited as can be seen from the Fast Fourier Transforms and time histories of responses obtained from experiments. However, both simulations and experiments showed similar qualitative characteristics.

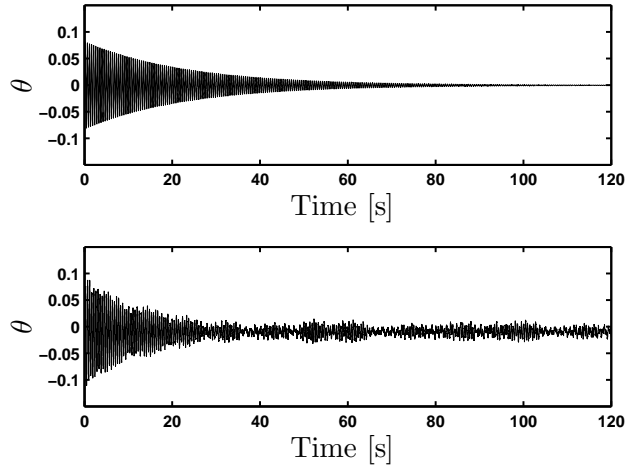


Figure 3.2: Comparison between time responses obtained from the simulations (top) and experiments (bottom) at a drive frequency of $\Omega = 0.9(2\pi) \text{ rad/s}$ with $A = 0$ during forward whirling.

The Fast Fourier Transforms of the torsion strain obtained from simulations and experiments during forward whirling and continuous rotor-stator contact at a drive frequency of $\Omega = 0.9(2\pi) \text{ rad/s}$ and various secondary frequencies are shown in Figure 3.6. For the experimental part, the drive speed was fixed, the secondary frequency amplitude was also fixed at 0.1Ω and the secondary frequency was changed in 0.2 Hz increments between 0.2 Hz to 10 Hz. At each secondary frequency addition experiment, the data was saved for 60 seconds after steady state was reached. The

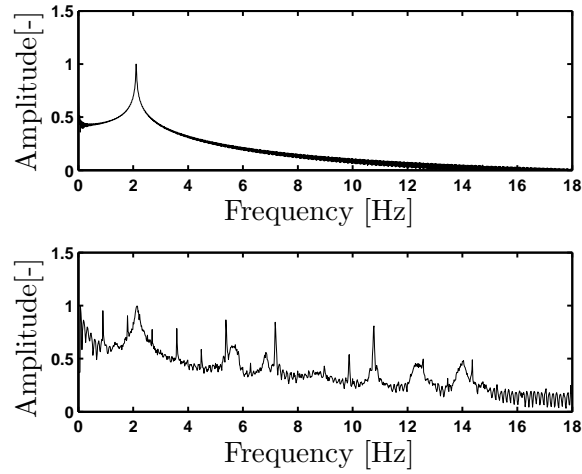


Figure 3.3: Comparison between Fast Fourier Transforms (FFTs) of the responses obtained from the simulations (top) and experiments (bottom) at a drive frequency of $\Omega = 0.9(2\pi)$ *rad/s* with $A = 0$ during forward whirling.

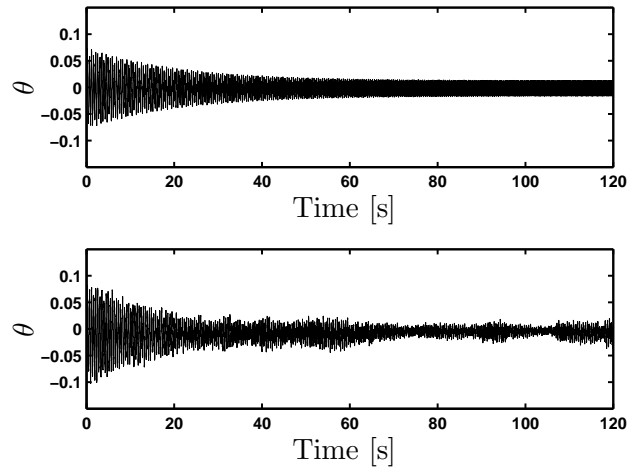


Figure 3.4: Comparison between time responses obtained from the simulations (top) and experiments (bottom) at a drive frequency of $\Omega = 0.9(2\pi)$ *rad/s* with $A = 0.1\Omega$ and $\alpha = 7.2(2\pi)$ *rad/s* during forward whirling.

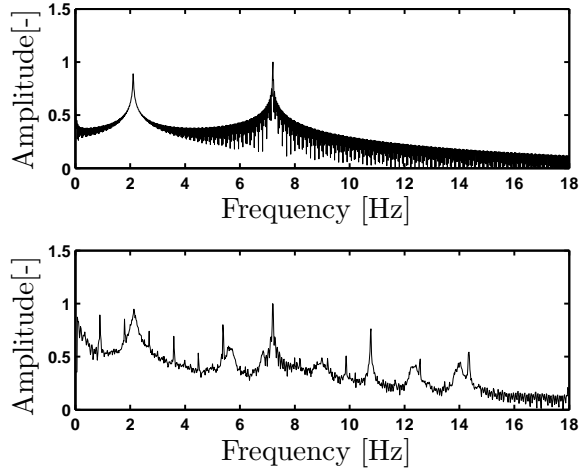
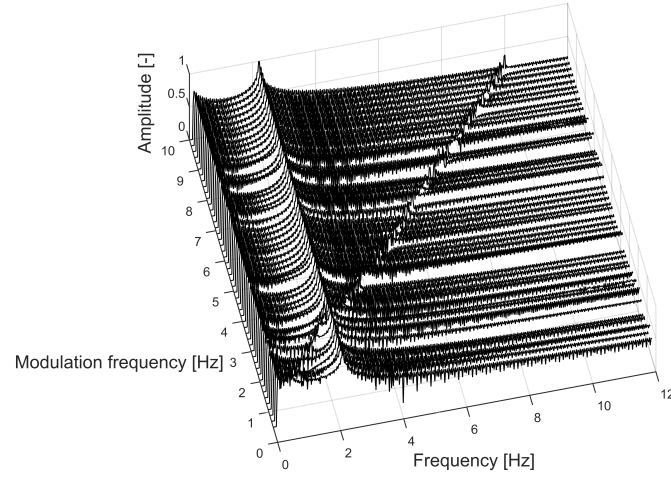


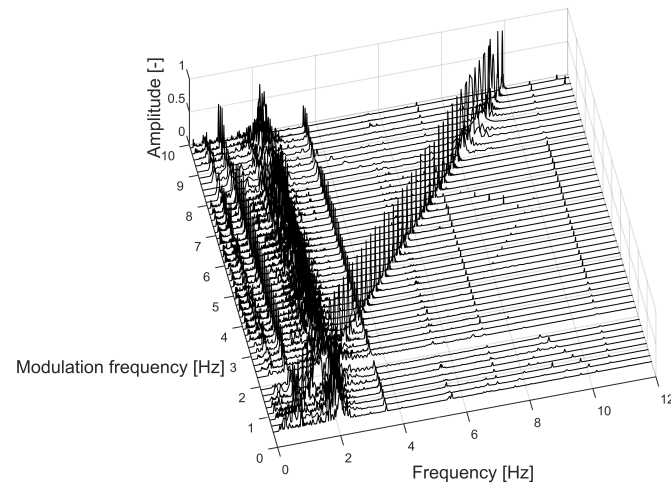
Figure 3.5: Comparison between Fast Fourier Transforms (FFTs) of the responses obtained from the simulations (top) and experiments (bottom) at a drive frequency of $\Omega = 0.9(2\pi) \text{ rad/s}$ with $A = 0.1\Omega$ and $\alpha = 7.2(2\pi) \text{ rad/s}$ during forward whirling. same procedure was performed for the numerical simulations and similarly the data was saved for 60 seconds after steady state conditions were reached. However, for the experimental part, the running of the experiments with a secondary frequency $\alpha \approx w_{nt}$ was avoided because of the close proximity to the first torsion natural frequency and avoid potential damage to the setup. For both simulations and experiments, the frequency spectra amplitude was normalized by dividing by the largest amplitude.

As seen in the numerical simulations, the main frequency components are at the secondary frequency and at the first torsion natural frequency. However, for the experimental results the dominant frequencies were at Ω , 4Ω , w_{nt} , and at α . The numerical simulations were not able to capture the contributions at Ω and 4Ω . Vlajic *et al.* [30] used a reduced order continuous rotor model with gyroscopic effects. The results contained these frequency components in the Fourier spectra,

this suggests that using a continuous rotor model with gyroscopic effects may be more appropriate.



(a)



(b)

Figure 3.6: Normalized Fourier spectra of torsion displacement response during forward whirling. a) Simulations and b) Experiments.

3.2.2 Lateral Vibrations

The x -position and y -position of the center of the rotor were measured by using a camera and tracking a white dot located at the center of the rotor. The time histories of the x -position of the rotor during forward whirling and continuous rotor-stator contact at a drive frequency of $\Omega = 0.9(2\pi) \text{ rad/s}$ obtained from both simulations and experiments are shown in Figure 3.7. The Fast Fourier Transforms for responses obtained from both simulations and experiments are shown in Figure 3.8 and the associated whirl orbits are shown in Figure 3.9. The lateral deflection responses obtained from simulations and experiments show close resemblance and both have the same dominant frequency component at $\Omega = 0.9(2\pi) \text{ rad/s}$.

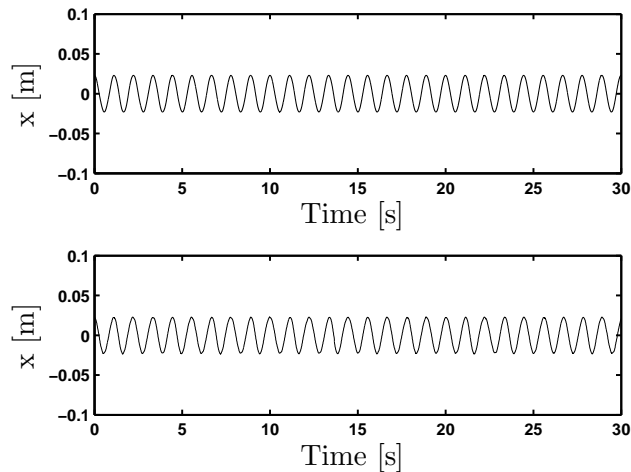


Figure 3.7: Comparison of the rotor center x -deflection obtained from the simulations (top) and experiments (bottom) at a drive frequency of $\Omega = 0.9(2\pi) \text{ rad/s}$ with $A = 0$ during forward whirling.

The time histories and their Fast Fourier Transforms for a drive frequency of

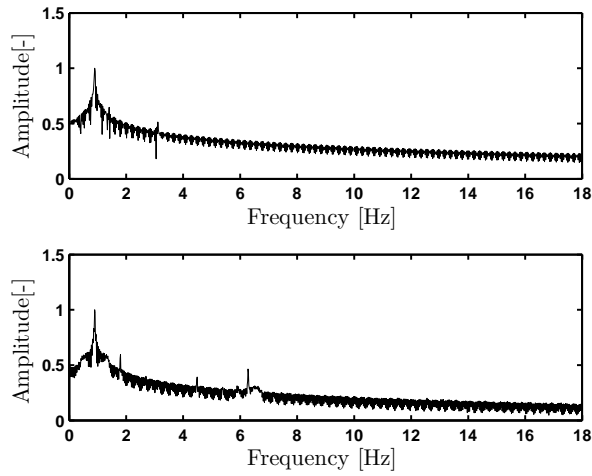


Figure 3.8: Comparison of Fast Fourier Transforms (FFTs) of the rotor center x -deflection obtained from the simulations (top) and experiments (bottom) at a drive frequency of $\Omega = 0.9(2\pi) \text{ rad/s}$ with $A = 0$ during forward whirling.

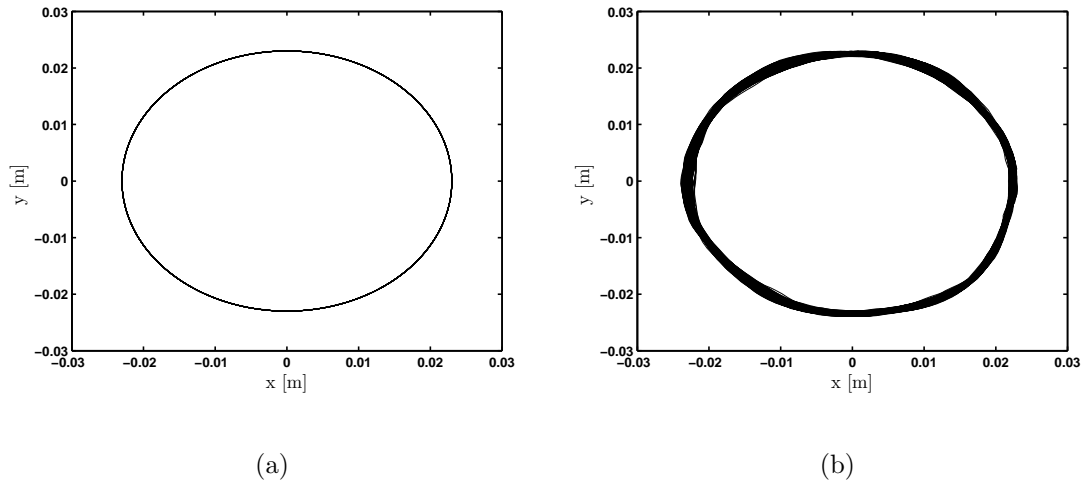


Figure 3.9: Whirl orbit during forward whirling with $\Omega = 0.9(2\pi) \text{ rad/s}$. a) Simulations and b) Experiments.

$\Omega = 0.9(2\pi) \text{ rad/s}$ modulated by a frequency of $\alpha = 7.2(2\pi) \text{ rad/s}$ are shown in Figures 3.10 and 3.11. The whirl orbits that the center of the rotor makes during this motion are shown in Figure 3.12. As seen from the figures, the dominant frequencies

in the responses are also at the drive frequency. However, the secondary frequency component in both experiments and simulations is not noticeable.

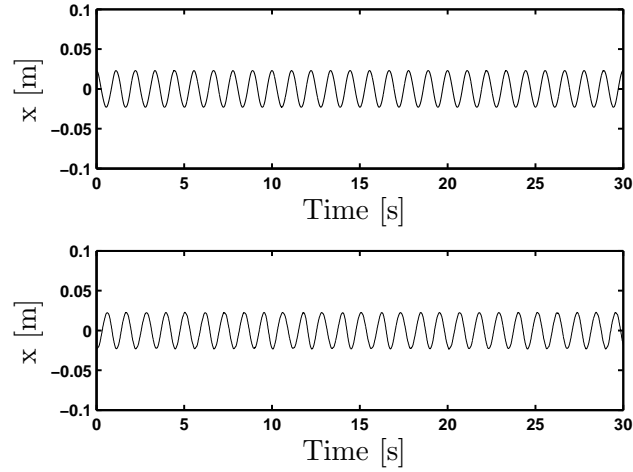


Figure 3.10: Comparison of the rotor center x -deflection obtained from the simulations (top) and experiments (bottom) at a drive frequency of $\Omega = 0.9(2\pi)$ rad/s , $A = 0.1\Omega$, and $\alpha = 7.2(2\pi)$ rad/s during forward whirling.

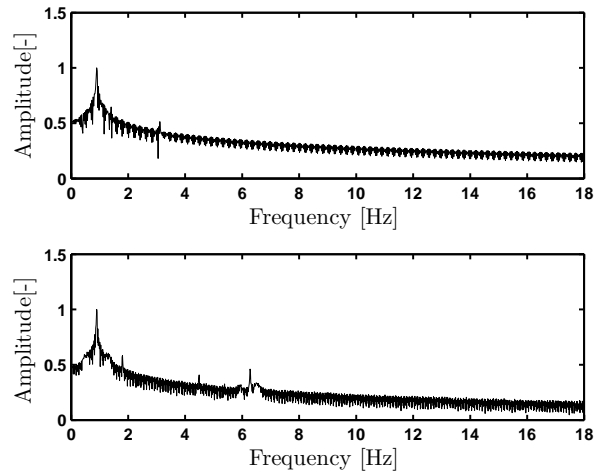


Figure 3.11: Comparison of Fast Fourier Transforms (FFTs) of the rotor center x -deflection obtained from the simulations (top) and experiments (bottom) at a drive frequency of $\Omega = 0.9(2\pi) \text{ rad/s}$, $A = 0.1\Omega$, and $\alpha = 7.2(2\pi) \text{ rad/s}$ during forward whirling.

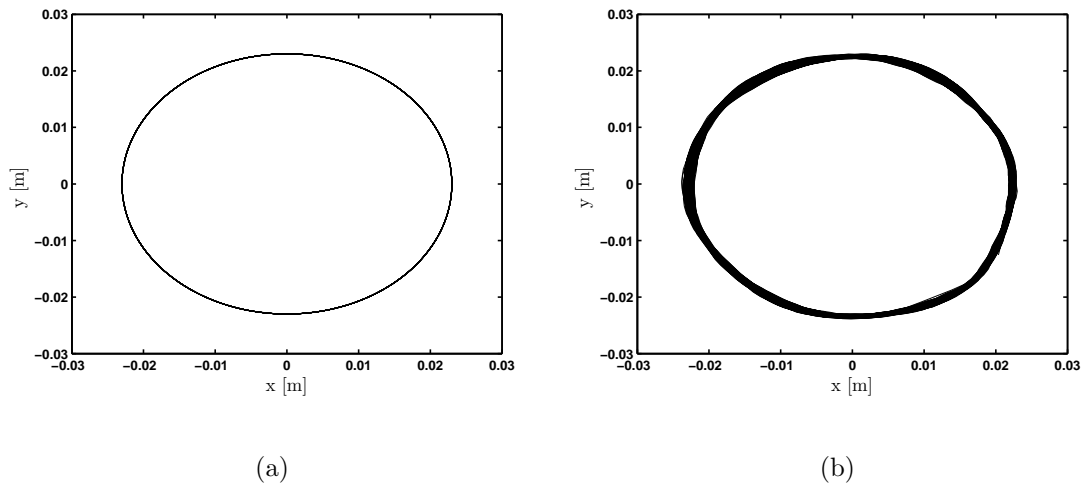


Figure 3.12: Whirl orbit during forward whirling with $\Omega = 0.9(2\pi) \text{ rad/s}$, $A = 0.1\Omega$, and $\alpha = 7.2(2\pi) \text{ rad/s}$. a) Simulations and b) Experiments.

3.3 Backward Whirling

3.3.1 Torsion Vibrations

To validate the model given by equation (2.21) for a backward whirling rotor during continuous rotor-stator contact, the system was first driven at a constant drive speed and was pushed into backward whirling. Similar to the forward whirling experiments, a step input was added through the motor drive speed to replicate the initial conditions in the simulations. The range of speeds at which the rotor remained in contact with the stator during backward whirling is approximately $\Omega > 0.23(2\pi)$ *rad/s* (≈ 13) rpm, which is close to the contact speed conditions derivable from the work of Bartha [31].

The drive speed was set to 36 rpm (0.6 Hz) at which the relative whirl speed was around 162 rpm (2.7 Hz). The relative whirl frequency of $\gamma = 2.7(2\pi)$ *rad/s* is of the same order of the first torsion natural frequency ($w_{nt} = 2.1(2\pi)$ *rad/s*). Therefore, this represents the slow whirling case. The Fast Fourier Transforms presented here are obtained following the same procedure as in the case of forward whirling; that is, by collecting at least 30 data segments of 40 seconds each, and then averaging FFTs obtained for the different time segments of steady state motions. A simulations-experiments comparison between the time histories and the Fast Fourier Transforms during backward whirling without drive speed modulation is shown in Figures 3.13 and 3.14. The responses obtained in both the simulations and experiments have the same dominant peak at $\gamma = 2.7(2\pi)$ *rad/s*. However,

the results obtained from the experiments showed multiple relatively low amplitude peaks at harmonics of the drive frequency.

To obtain the results shown in Figure 3.15 and 3.16, the drive speed was modulated with an input whose frequency is a multiple of the relative whirl frequency ($\alpha = 6\gamma = 16.2(2\pi) \text{ rad/s}$) and amplitude of $A = 0.1\Omega$. To compare the experimental data with the simulation results, both time histories and their associated Fast Fourier Transforms were used. As can be seen from the figures, the main peaks correspond to the relative whirl frequency of $\gamma = 2.7(2\pi) \text{ rad/s}$ in addition to the high excitation frequency α . As seen in the frequency spectra of the experimentally observed responses, in addition to the frequencies 5.4 Hz, 9.6 Hz, and 14.3 Hz, many other components were present that are not observed in the simulations, for similar reasons as described in the previous section. However, the respective spectral component amplitudes are small, and overall, both the responses observed in the simulations and experiments are found to be qualitatively similar. Additionally, due to the excessive speeds and stresses, the high speed backward whirling case was not experimentally studied.

The torsion strains obtained from the numerical and experimental studies during backward whirling are shown in Figure 3.17. In both the numerical and experimental studies, the drive speed was set to 36 rpm (0.6 Hz) and the secondary frequency amplitude was set to $A = 0.2\Omega$. For both the numerical and experimental studies, the relative whirl frequency was $\gamma \approx 4.5\Omega$, and the secondary frequency was changed in increments of 0.2 Hz for α in the range of $[0.2 - 10](2\pi) \text{ rad/s}$. In both simulations and experiments, the data were saved after the system reached

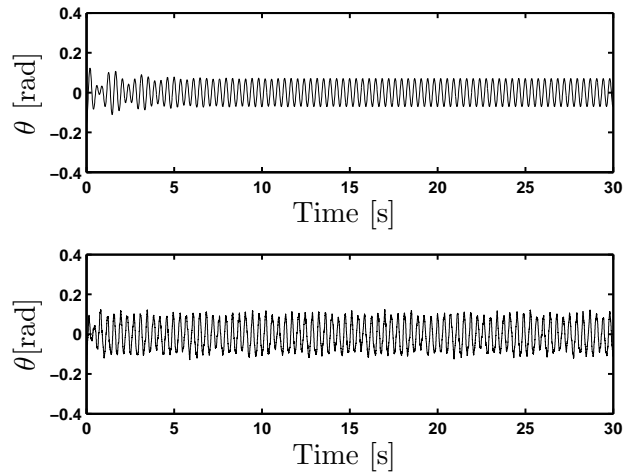


Figure 3.13: Comparison between time responses obtained from the simulations (top) and experiments (bottom) at a drive frequency of $\Omega = 0.6(2\pi)$ *rad/s* with $A = 0$ during backward whirling.

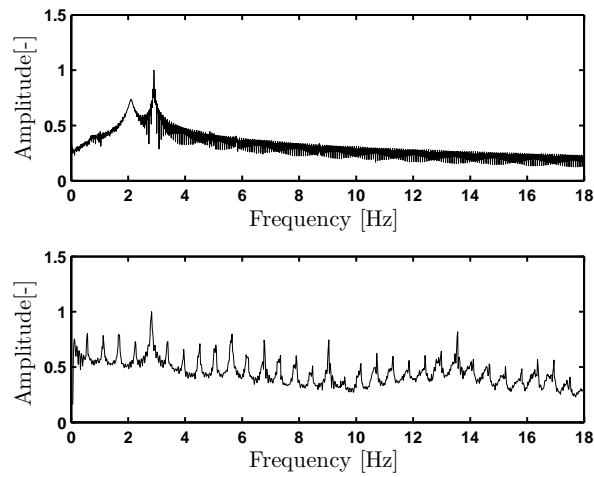


Figure 3.14: Comparison between Fast Fourier Transforms (FFTs) of the responses obtained from the simulations (top) and experiments (bottom) at a drive frequency of $\Omega = 0.6(2\pi)$ *rad/s* with $A = 0$ during backward whirling.

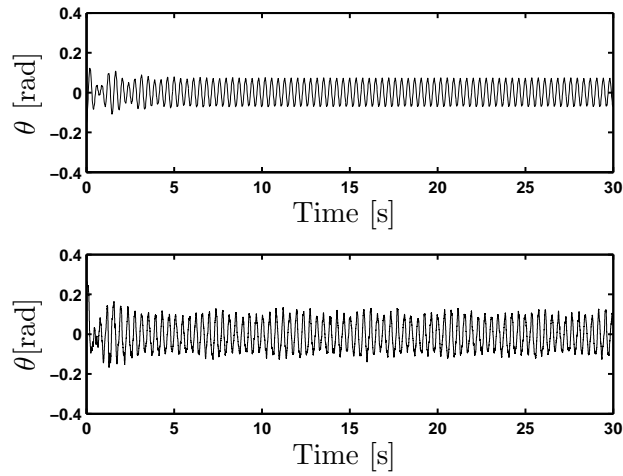


Figure 3.15: Comparison between time responses obtained from the simulations (top) and experiments (bottom) at a drive frequency of $\Omega = 0.6(2\pi)$ *rad/s* with $A = 0.1\Omega$ and $\alpha = 16.2(2\pi)$ *rad/s* during backward whirling.

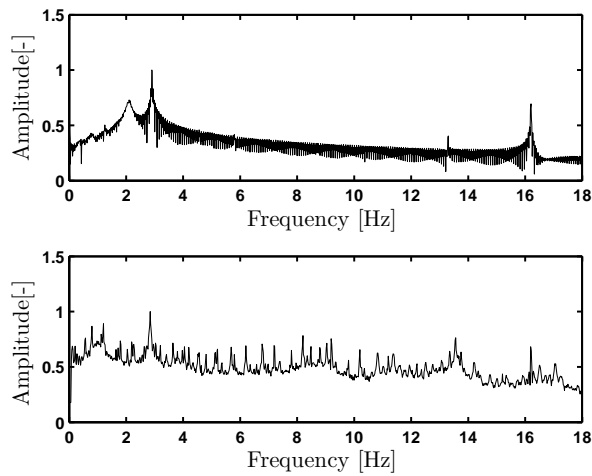


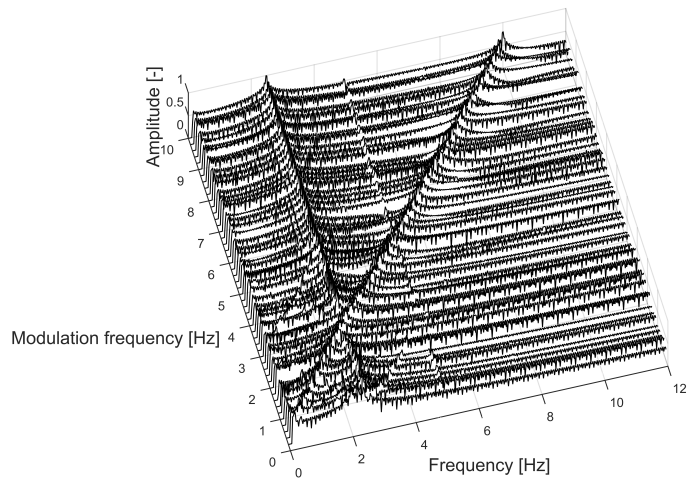
Figure 3.16: Comparison between Fast Fourier Transforms (FFTs) of the responses obtained from the simulations (top) and experiments (bottom) at a drive frequency of $\Omega = 0.6(2\pi)$ *rad/s* with $A = 0.1\Omega$ and $\alpha = 16.2(2\pi)$ *rad/s* during backward whirling.

steady state and for 60 seconds. Additionally, a secondary frequency addition close or equal to the first torsion natural frequency was avoided in the experiments to avoid structural damage. The spectral amplitude was also normalized by dividing throughout with the largest amplitude in both simulations and experimental results.

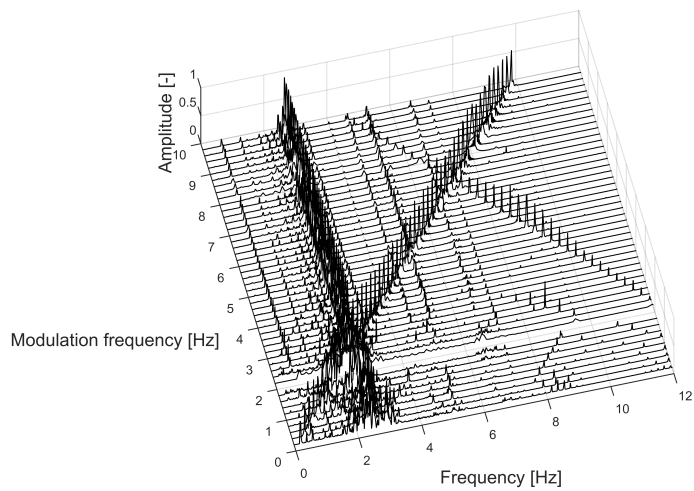
For the results shown in Figure 3.17, comparing the dominant frequency components for the simulations and experiments. The main spectral components for the responses obtained through the simulations are at γ , 2γ , and α while for the experimentally observed responses, the dominant frequencies are at γ , 2γ , Ω , $2\omega_{nt}$, and α . A significant component can be seen in the experimental response spectra which changes linearly with the secondary frequency as follows: $f = (14.19 - \alpha)(2\pi)$ *rad/s*. Both simulations and experiments results show good correlation for the main dominant frequencies. However, the components at Ω , 2Ω , $2\omega_{nt}$, and at $f = (14.19 - \alpha)(2\pi)$ *rad/s* are not present in the simulation results. The frequency spectra of the reduced order gyroscopic distributed parameter model derived by Vlajic *et al.* [30] for different drive speeds contained the frequency components at Ω and 2Ω which suggests the use of a similar model with the addition of secondary frequencies for more accurate results.

3.3.2 Hysteresis

During backward whirling and continuous rotor-stator contact, the rotor response may exhibit a hysteresis phenomenon. When increasing the drive speed of the motor gradually, the torsion displacement increases as the drive speed reaches a



(a)



(b)

Figure 3.17: Normalized Fourier spectra of the torsion displacement response during backward whirling. a) Simulations and b) Experiments.

frequency of 0.51 Hz (≈ 31 rpm). This frequency is close to both the first bending natural frequency ω_{nb} and a resonance due to gyroscopic forces that occurs when the whirl speed is half the torsion natural frequency, see Vlajic [2]. Then the torsion

displacement amplitude almost remains the same while further increasing the drive speed up to a certain point after which a jump happens in the torsion displacement. The amplitude after the jump down is much smaller than before and if the drive speed is slowly decreased, the torsion displacement does not follow the same path. Instead, the torsion displacement remains relatively small and increases again as the drive speed approaches the first critical speed. This hysteresis phenomenon was observed in measurements of actual drill-string vibrations. For an analytical study on the stability of periodic solutions during whirling motions of drill strings, the reader is referred to the work by Leine *et al.* [9].

The drive speed was incrementally increased up till the jump was observed and then decreased in 0.5 rpm increments for both up and down sweeps. At each location, the data was then recorded after 20 seconds and saved for about 30 seconds at each drive speed. The maximum steady state torsion displacement at each drive speed is shown in Figure 3.18. As seen in the figure, the jump is apparent at a drive speed of 40 rpm after which the speed was decreased and the maximum amplitude is seen to rise to the same level that it was initially at.

The Fast Fourier Transforms of the torsion time histories at each drive speed are shown in Figure 3.19. The frequency spectra shows that the system is oscillating with a frequency coincident with the first torsion natural frequency ($\omega_{nt} = 2.1(2\pi)$ rad/s) up to the jump point. After the jump, the torsion oscillation frequency is the same as the relative whirl frequency ($\gamma = \frac{R+\delta}{\delta}\Omega$) until the relative whirl frequency coincides with the first torsion natural frequency.

The response time history observed during a jump at a drive speed of 39 rpm is

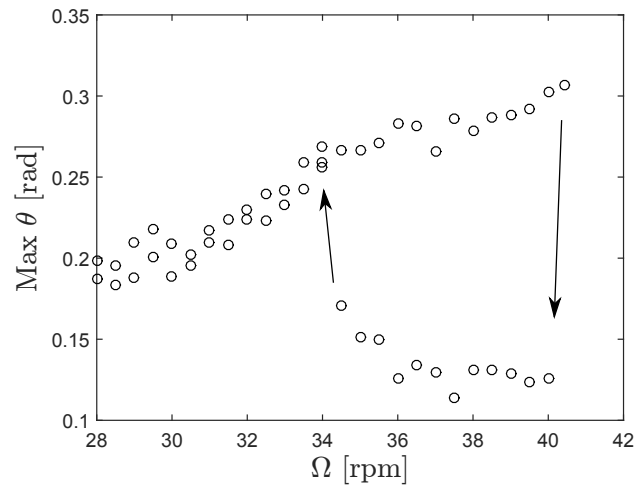


Figure 3.18: Change in the maximum amplitude of torsion displacement during a sweep-up, sweep-down test during backward whirling.

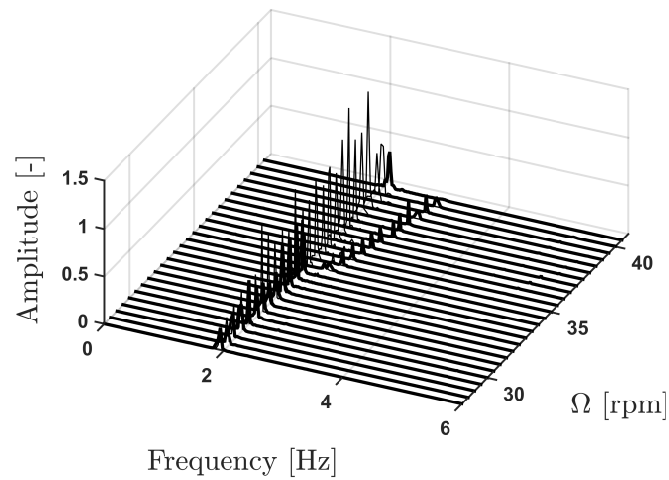


Figure 3.19: Frequency spectra of torsion displacement during a sweep-up, sweep-down test during backward whirling (bold lines correspond to the down-sweep).

shown in Figure 3.20. As seen in the figure after the jump, the oscillation amplitudes become small and the system response does not jump back to the previous state.

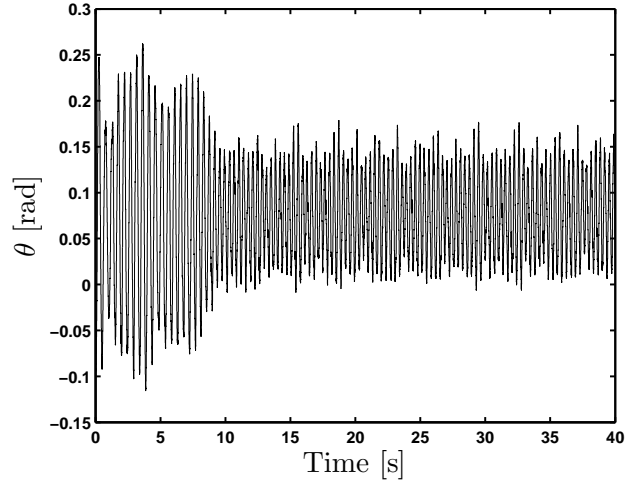


Figure 3.20: Time history of torsion amplitude during a jump at a drive speed of 39 rpm.

3.3.3 Lateral Vibrations

The lateral deflections of the center of the rotor at $\Omega = 0.67(2\pi) \text{ rad/s}$ and $\gamma \approx 3.0(2\pi) \text{ rad/s}$ during backward whirling and continuous rotor-stator contact of the simulations and experiments have also been studied. The time histories of the x -deflection of the rotor center and its Fast Fourier Transforms are shown in Figures 3.21 and 3.22. The whirl orbits that the center of the rotor makes in both experiments and simulations are shown in Figure 3.23. As shown in the figures, the time histories show very good resemblance and both simulations and experiments have the same frequency components at the whirl frequency $f_w = \gamma - f_d$ and at $\approx 2f_w$. Additionally, the experimentally observed frequency spectra contains multiple harmonics of f_w .

The x -position of the center of the rotor and the associated Fast Fourier

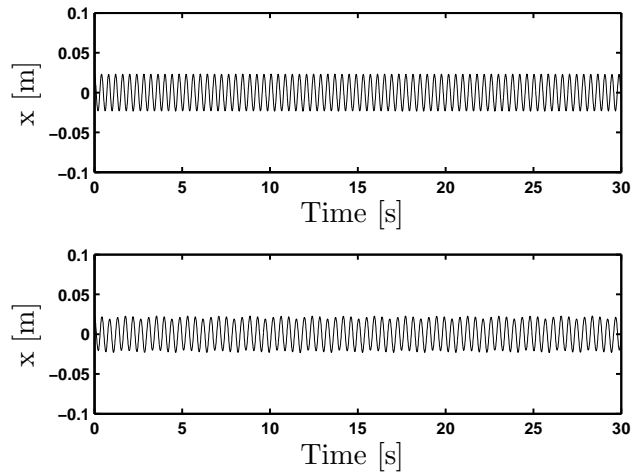


Figure 3.21: Comparison of the rotor center x -deflection obtained from the simulations (top) and experiments (bottom) at a drive frequency of $\Omega = 0.67(2\pi) \text{ rad/s}$ with $A = 0$ during backward whirling.

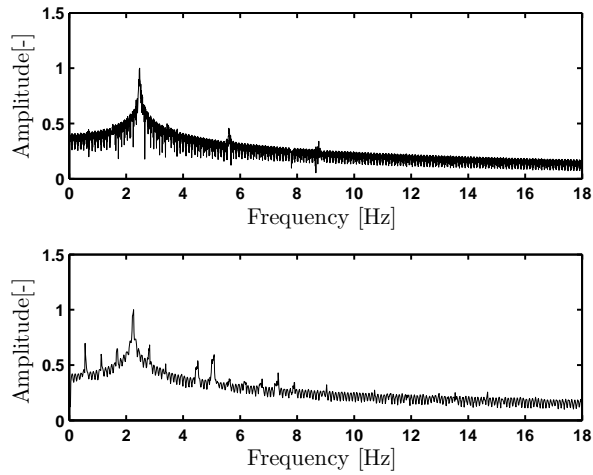


Figure 3.22: Comparison of Fast Fourier Transforms (FFTs) of the rotor center x -deflection obtained from the simulations (top) and experiments (bottom) at a drive frequency of $\Omega = 0.67(2\pi) \text{ rad/s}$ with $A = 0$ during backward whirling.

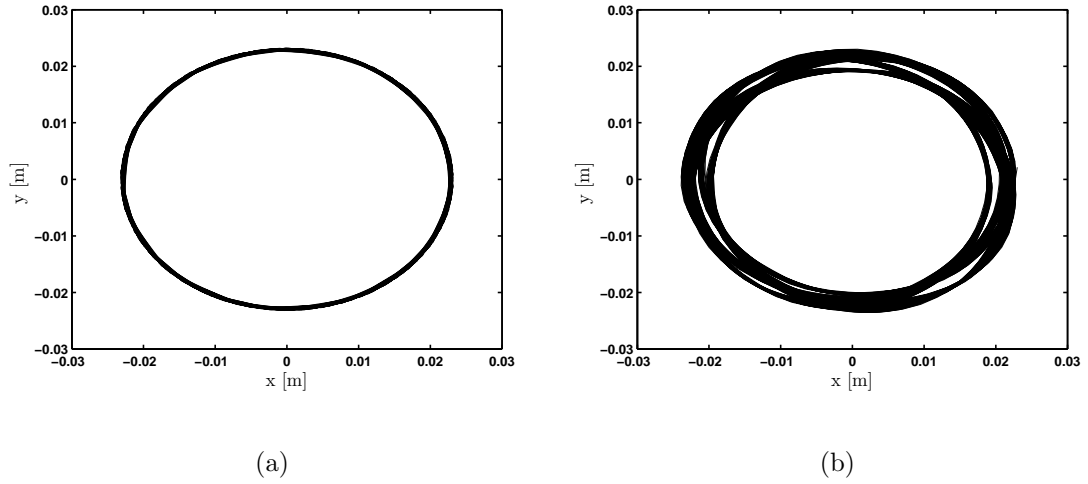


Figure 3.23: Whirl orbit during backward whirling with $\Omega = 0.67(2\pi) \text{ rad/s}$. a) Simulations and b) Experiments.

Transform at a drive frequency of $\Omega = 0.67(2\pi) \text{ rad/s}$, modulation amplitude of $A = 0.1\Omega$, and a modulation frequency of $\alpha = 16.2(2\pi) \text{ rad/s}$ are shown in Figures 3.24 and 3.25. The whirl orbits observed in both experiments and simulations are shown in Figure 3.26. As can be seen in the figures, the responses observed in experiments and simulations have the same dominant peaks again at $f_w = \gamma - f_d$ and the experiment shows multiple harmonics at multiples of the drive speed. Interestingly, similar to the forward whirling case, neither simulations or experiments contained a frequency component at the excitation frequency $\alpha = 16.2(2\pi) \text{ rad/s}$. Furthermore, in both experiments and simulations, the rotor response followed a circular whirl orbit. However, the thickness of the whirl orbits in the experiments is larger than the ones observed in the simulations.

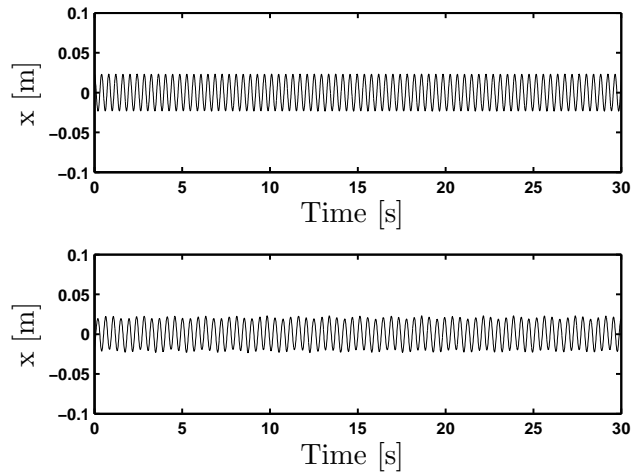


Figure 3.24: Comparison of the rotor center x -deflection obtained from the simulations (top) and experiments (bottom) at a drive frequency of $\Omega = 0.67(2\pi) \text{ rad/s}$ with $A = 0.1\Omega$, and $\alpha = 16.2(2\pi) \text{ rad/s}$ during backward whirling.

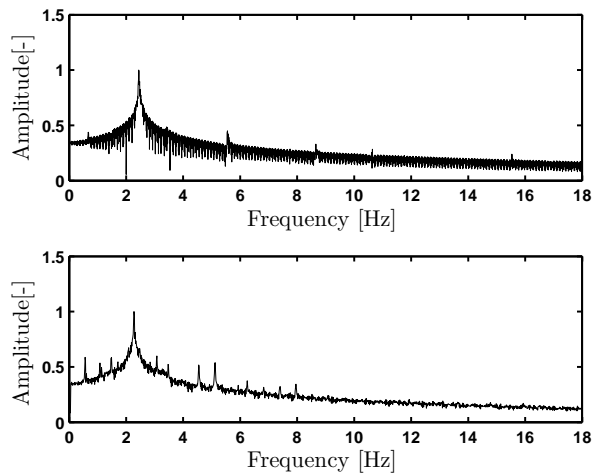


Figure 3.25: Comparison of Fast Fourier Transforms (FFTs) of the rotor center x -deflection obtained from the simulations (top) and experiments (bottom) at a drive frequency of $\Omega = 0.67(2\pi) \text{ rad/s}$ with $A = 0.1\Omega$, and $\alpha = 16.2(2\pi) \text{ rad/s}$ during backward whirling.

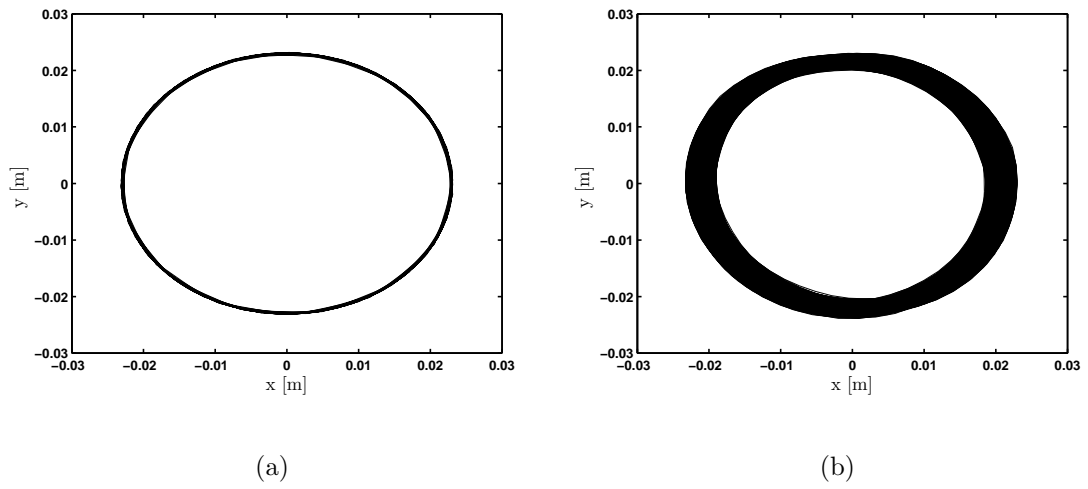


Figure 3.26: Whirl orbit during backward whirling with $\Omega = 0.67(2\pi) \text{ rad/s}$, $A = 0.1\Omega$, and $\alpha = 16.2(2\pi) \text{ rad/s}$. a) Simulations and b) Experiments.

Chapter 4: Summary and Future Work

4.1 Summary and Conclusions

A drill string which is an example of a slender, rotating structure has been modeled as an extended Jeffcott rotor. The drive speed of the rotor was modulated by a sinusoidal signal and a reduced-order model was constructed to study the torsion vibrations during continuous rotor-stator contact during forward and backward whirling.

Analytical findings showed that the equivalent torsion stiffness increased and that the discontinuity in the friction coefficient was smoothed for both forward and backward whirling. The experimental results showed good qualitative agreement with the response of the developed models. However, in the current experimental setup, it is difficult to observe whether there was any stiffening effect or if the friction force changed due to the drive speed modulation. Some of the key findings of the analytical-numerical study are as follows:

1. High frequency modulation of the drive speed caused the jump discontinuity in the friction force to be smoothed with increasing modulation amplitude
2. From the results of the analysis, the modulation increased the equivalent stiff-

ness of the torsion mode during continuous rotor-stator contact.

3. The velocity weakening effect in the friction coefficient or torque models of drill strings has a large impact on the stick-slip vibrations observed for constant drive speeds [19, 32]. The smoothing of the discontinuity and the reduction of the regions of negative slope in the friction force suggest that the high frequency modulation of the drive speed can have a beneficial effect in quenching self-excited vibrations present in many rotor systems.

A scaled drill-string experimental apparatus was used to generate results and compare with predictions from models used in this work. The main outcomes of the experimental study are as follows:

1. Time histories of the torsion response of both simulations and experiments showed similar qualitative properties away from the system resonances with and without drive speed modulation.
2. The frequency spectra of the simulations of the torsional responses for a secondary frequency sweep over a constant drive speed was compared to that obtained from experiments during forward and backward whirling. Both responses observed in simulations and experiments had the same dominant peaks. However, the responses obtained in the simulations did not contain multiple frequency components that were present in the experimentally observed responses.
3. A frequency component of $f = (14.19 - \alpha)$ Hz appeared in the experiments

during continuous rotor-stator contact and backward whirling. The reason for the presence of this frequency was not further studied in this work.

4. The lateral responses observed in simulations with the extended Jeffcott rotor model and the experiments showed strong resemblance. Additionally, the data showed that the impact of drive speed modulation on the lateral motion during continuous rotor-stator contact is barely noticeable.
5. A resonance of the first torsion mode at twice the rotor relative whirl speed was observed in the experiments. This resonance was not picked up in simulations of the extended Jeffcott model. However, Vlajic [2] studied torsion motions of such a system and concluded that this resonance is due to gyroscopic effects. Therefore, including gyroscopic effects in the model will need consideration.

4.2 Recommendations For Future Work

Further experimental and analytical work is needed to fully understand the effects of drive speed modulation. Additionally, the effect of high frequency excitation on quenching self-excited torsion vibrations in rotating structures needs further investigation, both numerically and experimentally.

This work can be extended to study the effects of drive speed modulation on a distributed parameter drill string model with gyroscopic effects, and to study the effects of drive speed modulation on a rotor whirling without contact and on a rotor undergoing impact motions. Additionally, the effects of drive speed modulations with low frequencies and different modulation functions on the dynamics of rotor

systems can be studied.

Appendix A: MATLAB Codes

Representative codes used in this thesis are included in this appendix.

```

% This code compares the response between the reduced
torsional equation
% and the extended Jeffcott rotor model

%% System Parameters:

Mass_rotor          =0.625;
mass_unbalance      =0.08;
e                   =0.0635;
delta               =0.023;
zeta                =0.0032;
zetab               =0.008;
R                   =0.088;
J
= (Mass_rotor)*R^2/2+(mass_unbalance)*e^2;
kb
= (0.5125*2*pi)^2*(Mass_rotor+mass_unbalance);
kt
= (2.1*2*pi)^2*J;
ks                  =100000;
cb                  =0.0000;
wn_t                =sqrt(kt/J);
wn_t_hz             =wn_t/(2*pi)
wn_b                =sqrt(kb/(Mass_rotor+mass_unbalance));
wn_b_hz             =sqrt(kb/(Mass_rotor+mass_unbalance))/(2*pi)
ct                  =2*zeta*J*wn_t;
cb
=2*zetab*(Mass_rotor+mass_unbalance)*wn_b;

M=Mass_rotor;
m=mass_unbalance;
a=-R/delta; %Backward
% a=1; %Forward

%Input
Omega =54*pi/30;
alpha =Omega*8;
A      =Omega*0.0;

%Friction Model
Mu_m=0.005;
Mu_s=1.300*Mu_m;
vm=0.6;

```

```

Mu1=3/2*(Mu_s-Mu_m)/vm;
Mu3=1/2*(Mu_s-Mu_m)/vm^3;

Parameters=[J,M,m,e,delta,c,kt,Omega,alpha,A,Mu1,Mu3,R,Mu_s
, kb, ks, cb, vm, Mu_m, Mu_s];

%% ODE
time_s=[120];

theta_0_red=[0.1 0];
theta_0_full=[delta 0 0.1 0.0 delta*Omega 0];

Sol_red = ode45(@torsional,[0
time_s],theta_0_red,[],Parameters);
timeVec1 = linspace(0,time_s,20000);
Sol_red1 = deval(Sol_red,timeVec1);

theta_red =Sol_red1(1,:);
theta_red_dot=Sol_red1(2,:);

Sol_full = ode15s(@fullwithforces,[0
time_s],theta_0_full,[],Parameters);
t = linspace(0,time_s,20000);
Sol_full2 = deval(Sol_full,t);

theta_full =Sol_full2(3,:);
theta_dot_full =Sol_full2(6,:);
x =Sol_full2(1,:);
y =Sol_full2(2,:);
x_dot =Sol_full2(4,:);

%% Fast Fourier Transform

x_full=(theta_full(round(length(theta_full))*0.5:length(theta_
ta_full)));
x_red=(theta_red(round(length(theta_red))*0.5:length(theta_
red)));

fs_full=1/(t(10)-t(9));
fs_red=fs_full;

m_full = length(x_full);
m_red = length(x_red);

```

```

n_full = pow2(nextpow2(m_full));
n_red = pow2(nextpow2(m_red));

x_full_fft=fft(x_full,n_full);
x_red_fft=fft(x_red,n_red);

power_x_full=x_full_fft.*conj(x_full_fft)/n_full;
power_x_red=x_red_fft.*conj(x_red_fft)/n_red;

f_full = (0:n_full-1)*(fs_full/n_full);
f_red = (0:n_red-1)*(fs_red/n_red);

PXF=power_x_full+1;
LPF=log(PXF);
LPmaxF=max(LPF);
LPnormF=LPF/LPmaxF;

PXR=power_x_red+1;
LPR=log(PXR);
LPmaxR=max(LPR);
LPnormR=LPR/LPmaxR;

R1=(log(LPnormR));
RR=R1+abs(min(R1));
LR1=RR/max(RR); %normalized

F1=(log(LPnormF));
FF=F1+abs(min(F1));
LF1=FF/max(FF); %normalized

```



```
% Function file for the reduced order torsional equation
```

```
function dx=torsionalFWD(t,x,Parameters)
```

```
dx=zeros(2,1);
```

```
J      =Parameters(1);
```

```
M      =Parameters(2);
```

```
m      =Parameters(3);
```

```
e      =Parameters(4);
```

```
delta  =Parameters(5);
```

```
c      =Parameters(6);
```

```
kt     =Parameters(7);
```

```
Omega  =Parameters(8);
```

```
alpha  =Parameters(9);
```

```
A      =Parameters(10);
```

```
Mu1    =Parameters(11);
```

```
Mu3    =Parameters(12);
```

```
R      =Parameters(13);
```

```
Mu_s   =Parameters(14);
```

```
kb     =Parameters(15);
```

```
ks     =Parameters(16);
```

```
cb     =Parameters(17);
```

```
vm     =Parameters(18);
```

```
Mu_m   =Parameters(19);
```

```
Mu_s   =Parameters(20);
```

```
a=1; % Forward whirling
```

```
%a=-R/delta; Backward whirling
```

```
dx(1)=x(2);
```

```
vrel=(delta+R)*(Omega+A*sin(alpha*t))+x(2)*R;
```

```
df=1e6;
```

```
muu=Mu_s*2/pi*atan(df*vrel)-3/2*(Mu_s-Mu_m)*(vrel/vm-  
1/3*(vrel/vm)^3);
```

```
Fn=(M+m)*delta*(Omega+A*sin(alpha*t))^2-kb*delta;
```

```
Ft=-muu*Fn;
```

```
Mt=Ft*R;
```

```
dx(2)=(-ct*(x(2))-
```

```
x(1)*(kt+m*e*(delta*a^2*(Omega+G_dot)^2*cos((a-  
1)*(Omega*t+G))-G_ddot*delta*a*sin((a-1)*(Omega*t+G)))-
```

```
...
```

```
m*e*(delta*a^2*(Omega+G_dot)^2*sin((a-1)*(Omega*t+G))-  
delta*a*G_ddot*cos((a-1)*(Omega*t+G)))-J*G_ddot+Mt)/J;
```

```
% Function file for the 3DOF extended Jeffcott rotor model
```

```
function dx = fullwithforces(t,x,Parameters)
```

```
dx = zeros(6,1);
```

```
% System Parameters
```

```
J      =Parameters(1);  
M      =Parameters(2);  
m      =Parameters(3);  
e      =Parameters(4);  
delta  =Parameters(5);  
ct     =Parameters(6);  
kt     =Parameters(7);  
Omega  =Parameters(8);  
alpha  =Parameters(9);  
A      =Parameters(10);  
Mu1    =Parameters(11);  
Mu3    =Parameters(12);  
R      =Parameters(13);  
Mu_s   =Parameters(14);  
kb     =Parameters(15);  
ks     =Parameters(16);  
cb     =Parameters(17);  
vm     =Parameters(18);  
Mu_m   =Parameters(19);  
Mu_s   =Parameters(20);
```

```
dx(1:3)      = x(4:6);
```

```
Beta      =(x(3)+Omega*t-A/alpha *cos(alpha*t));
```

```
Betadot   =(x(6)+Omega+A*sin(alpha*t));
```

```
rho       =sqrt(x(1)^2 + x(2)^2);
```

```
eta       =atan2(x(2),x(1));
```

```
s_eta     =sin(eta);
```

```
c_eta     =cos(eta);
```

```
vtan      =-x(4)*s_eta + x(5)*c_eta;
```

```
vrel      =(Omega+x(6)+A*sin(alpha*t))*R+vtan;
```

```
df=1e6;
```

```

    muu=Mu_s*atan(df*vrel)-3/2*(Mu_s-Mu_m)*(vrel/vm-
1/3*(vrel/vm)^3);

if rho <= delta
    lambda = 0;
    Fnormal = 0;
elseif rho >delta
    lambda = 1;
    Fnormal = ks*(rho-delta);
end

Ftan = -muu*sign(vrel)*Fnormal;
Fv    = -Ftan*s_eta - Fnormal*c_eta;
Fw    = Ftan*c_eta - Fnormal*s_eta;
Forces = lambda*[Fv Fw R*Ftan]';

Mass      = [ (M + m)      0      -
m*e*sin(Beta);
              0            (M + m)
m*e*cos(Beta);
              -m*e*sin(Beta)  m*e*cos(Beta)  J ];

Stiff     = [ kb*x(1);
              kb*x(2);
              kt*x(3) ];

Damp     = [ cb*x(4);
              cb*x(5);
              ct*x(6) ];

NonLin    = [
m*e*(Betadot)^2*cos(Beta)+m*e*A*alpha*cos(alpha*t)*sin(Beta
);
              m*e*(Betadot)^2*sin(Beta)-
m*e*A*alpha*cos(alpha*t)*cos(Beta);
              -J*A*alpha*cos(alpha*t) ];

dx(4:6)   = Mass\(-Stiff - Damp + NonLin + Forces);

```

```
%Image processing code used for tracking a white dot on the
rotor-center.
```

```
%Originally written by Nick Vlajic
```

```
file           = 'test.avi';
info           = aviinfo(file);
tmov           = mmreader(file);
nFrames        = info.NumFrames;
fRate          = info.FramesPerSecond;
dTime          = 1/fRate;
timeVec        = (0:nFrames-1)*dTime;

positionxPix   = nan(nFrames,1);
positionyPix   = nan(nFrames,1);
adjust         = 1.7;
arealim        = 10;

pix2mm         = 0.21;
%%
for ind1 = 1:nFrames-1

    disp(ind1)
    image       = read(tmov,ind1);
    imageCrop   = image(:, :, 1);
    level       = graythresh(imageCrop)*adjust;

    imageBW     = im2bw(imageCrop,level);
    [B,L] = bwboundaries(imageBW,4,'noholes');
    s = regionprops(L);

    for ind2 = 1:length(s);
        if s(ind2).Area > arealim
            positionxPix(ind1) = s(ind2).BoundingBox(1) +
s(ind2).BoundingBox(3)/2;
            positionyPix(ind1) = s(ind2).BoundingBox(2) +
s(ind2).BoundingBox(4)/2;
        end
    end
end

%%
pX            = (positionxPix)*pix2mm;
pY            = (positionyPix)*pix2mm;
savename      = [file '_VideoData.mat'];
```

Bibliography

- [1] Vlajic N. Karki H. Liao, C.M. and B. Balachandran. Parametric studies on drill-string motions. *International Journal of Mechanical Sciences*, 54(1):260–268, 2012.
- [2] N. Vlajic. Dynamics of slender, flexible structures. PhD Dissertation, University of Maryland, College Park, 2014.
- [3] N. Vlajic, C.M. Liao, H. Karki, and B. Balachandran. Stick-slip motions of a rotor-stator system. *Journal of Vibration and Acoustics*, 136(2):021005, 2014.
- [4] J.D. Jansen. Non-linear rotor dynamics as applied to oilwell drillstring vibrations. *Journal of Sound and Vibration*, 147(1):115–135, 1991.
- [5] L.F. Kreisle and J.M. Vance. Mathematical analysis of the effect of a shock sub on the longitudinal vibrations of an oilwell drill string. *Society of Petroleum Engineers Journal*, 10(04):349–356, 1970.

- [6] J.D. Jansen and L. Van den Steen. Active damping of self-excited torsional vibrations in oil well drillstrings. *Journal of Sound and Vibration*, 179(4):647–668, 1995.
- [7] Piovan M.T. Sampaio, R. and G.V. Lozano. Coupled axial/torsional vibrations of drill-strings by means of non-linear model. *Mechanics Research Communications*, 34(5):497–502, 2007.
- [8] A.S. Yigit and A.P. Christoforou. Coupled axial and transverse vibrations of oilwell drillstrings. *Journal of Sound and Vibration*, 195(4):617–627, 1996.
- [9] Van Campen D.H. Leine, R.I. and W.J.G. Keultjes. Stick-slip whirl interaction in drillstring dynamics. *Journal of Vibration and Acoustics*, 124(2):209–220, 2002.
- [10] E. Kreuzer and M. Steidl. Model order reduction of a drill-string-model with self-excited stick-slip vibrations. *PAMM*, 9(1):295–296, 2009.
- [11] N. Vljajic, X. Liu, H. Karki, and B. Balachandran. Torsional oscillations of a rotor with continuous stator contact. *International Journal of Mechanical Sciences*, 83:65–75, 2014.
- [12] N. Mihajlovic. Torsional and lateral vibrations in flexible rotor systems with friction. PhD Dissertation, Technische Universiteit Eindhoven, 2005.
- [13] C.M. Liao. Experimental and numerical studies of drill-string dynamics. PhD Dissertation, University of Maryland, College Park, 2011.

- [14] N. Vljajic, C.M. Liao, H. Karki, and B. Balachandran. Stick-slip and whirl motions of drill strings: Numerical and experimental studies. In *ASME 2011 International Design Engineering Technical Conferences and Computers and Information in Engineering Conference*, pages 829–838. American Society of Mechanical Engineers, 2011.
- [15] N. Vljajic, T. Fitzgerald, V. Nguyen, and B. Balachandran. Geometrically exact planar beams with initial pre-stress and large curvature: Static configurations, natural frequencies, and mode shapes. *International Journal of Solids and Structures*, 51(19):3361–3371, 2014.
- [16] Gorelik I. Rudat J. Moritz C. Neubauer M. Wallaschek J. Hohn O. Westermann, H. A new test rig for experimental studies of drillstring vibrations. *SPE Drilling Completion*, 30(02):119–128, 2015.
- [17] M. Karkoub, M. Zribi, L. Elchaar, and L. Lamont. Robust μ -synthesis controllers for suppressing stick-slip induced vibrations in oil well drill strings. *Multibody System Dynamics*, 23(2):191–207, 2010.
- [18] Van de Molengraft M.J.G. Kok J.J. Serrarens, A.F.A. and L Van den Steen. H control for suppressing stick-slip in oil well drillstrings. *Control Systems, IEEE*, 18(2):19–30, 1998.
- [19] A.P. Christoforou and A.S. Yigit. Fully coupled vibrations of actively controlled drillstrings. *Journal of Sound and Vibration*, 267(5):1029–1045, 2003.

- [20] S.A. Al-Hiddabi, B. Samanta, and A. Seibi. Non-linear control of torsional and bending vibrations of oilwell drillstrings. *Journal of Sound and Vibration*, 265(2):401–415, 2003.
- [21] E. Kreuzer and M. Steidl. Controlling torsional vibrations of drill strings via decomposition of traveling waves. *Archive of Applied Mechanics*, 82(4):515–531, 2012.
- [22] G.W. Meyer. Investigations into the effects of secondary-frequency additions on slender rotating structures. MS thesis, University of Maryland, College Park, 2014.
- [23] J.J. Thomsen. *Vibrations and stability: advanced theory, analysis, and tools*. Springer Science & Business Media, 2003.
- [24] I.I. Blekhman. *Vibrational mechanics: nonlinear dynamic effects, general approach, applications*. World Scientific, 2000.
- [25] J.J. Thomsen. Using fast vibrations to quench friction-induced oscillations. *Journal of Sound and Vibration*, 228(5):1079–1102, 1999.
- [26] J.J. Thomsen. Slow high-frequency effects in mechanics: problems, solutions, potentials. *International Journal of Bifurcation and Chaos*, 15(09):2799–2818, 2005.
- [27] R. Leine and H. Nijmeijer. *Dynamics and bifurcations of non-smooth mechanical systems*, volume 18. Springer Science & Business Media, 2013.

- [28] A.H. Nayfeh and D.T. Mook. *Nonlinear oscillations*. John Wiley & Sons, 2008.
- [29] A.H. Nayfeh and B. Balachandran. *Applied nonlinear dynamics: analytical, computational and experimental methods*. John Wiley & Sons, 2008.
- [30] N. Vljajic, X. Liu, H. Karki, and B. Balachandran. Rotor torsion vibrations in the presence of continuous stator contact. In *ASME 2012 International Mechanical Engineering Congress and Exposition*, pages 785–794. American Society of Mechanical Engineers, 2012.
- [31] A.R. Bartha. Dry friction backward whirl of rotors. PhD Dissertation, Technische Wissenschaften ETH Zürich, Nr. 13817, 2001, 2000.
- [32] J.F. Brett. The genesis of bit-induced torsional drillstring vibrations. *SPE Drilling Engineering*, 7(03):168–174, 1992.